Wintertime In-situ Cloud Microphysical Properties of Mixed-phase Clouds over the Southern Ocean

Yi Huang[1,2], Steven T. Siems[2,3], and Michael J. Manton[3]

[1]School of Earth Sciences, The University of Melbourne, Melbourne, Australia.
[2]Australian Research Council (ARC) Centre of Excellence for Climate Extremes (CLEX)
[3]School of Earth, Atmosphere and Environment, Monash University, Melbourne, Australia.

Corresponding author: Yi Huang (yi.huang4@unimelb.edu.au)

Key Points:

- Mixed phase clouds are commonly present in mid-latitude mesoscale shallow convection over the Southern Ocean during the Austral winter.
- Secondary ice production, together with warm rain processes, is potentially important in producing ice particles in the supercooled clouds.
- Large discrepancies are found in the widely used satellite-based cloud phase products.

Abstract

In-situ observations made over twenty flights during three Austral winters (Jun–Oct, 2013–15) were analyzed to characterize the cloud microphysical properties and natural variability of mid-latitude shallow convective clouds over the Southern Ocean (SO), with a focus on pristine conditions and the mixed-phase temperature range (MPTR, 0ºC to -31ºC). Liquid, mixed-phase, and ice cloud fractions were observed 39%, 44%, and 17% of the time, respectively, under various meteorological settings. Liquid phase clouds were typically characterized by low droplet number concentrations and the common presence of drizzle. Supercooled liquid water was prevalent in the MPTR, while freezing of supercooled raindrops likely formed the primary ice nucleation mechanism in these shallow clouds. Ice particles of various habits were present in the mature/maturing convective cloud cells, suggesting the operation of multiple particle growth regimes. Increased ice particle concentrations (exceeding 100 L^{-1}), well in excess of the expected ice nuclei concentrations, were measured at temperature warmer than approximately -12℃, signaling the operation of secondary ice production mechanisms. However, these cloud segments were spatiotemporally inhomogeneous, suggesting the chaotic and turbulent nature of the secondary ice-forming processes. Accurately representing these processes in global models, while necessary, is likely a challenge. Our analysis also found marked inconsistencies between several satellite-based cloud phase products that have underpinned recent developments of model parameterization frameworks. Understanding and addressing these inconsistencies are critical towards improving the representation of SO clouds and their radiative properties in climate models.

Plain Language Summary

Mixed-phase consist of both supercooled cloud droplets and ice crystals. They exert significant controls on the energy balance, particularly over the Southern Ocean (SO). Current satellite products have difficulties in determining how often mixed-phase clouds are present over the remote SO, which leads to challenges in representing them in state-of-the-art weather and climate models, resulting in large uncertainties in future climate projections. In this study we use aircraft data from twenty flights to examine the mixed-phase cloud occurrences and their microphysical characteristics over the mid-latitude SO during Austral winter months. We explore and identify some processes that might be key to the formation and maintenance of mixed-phase clouds in shallow convection. We also employ these in-situ observations to better understand biases identified in satellite cloud phase products.

1. Introduction

Mixed phase cloud, where supercooled liquid droplets and ice crystals coexist, is an inherently unstable system, representing a theoretically fast transition from water to ice. Such instability allows for the rapid growth of ice crystals, often to precipitation sizes, on relative short time scales. However, mixed phase is commonly observed in clouds that extend above the freezing level. As such, it plays a critical role in modulating the life cycle of clouds, precipitation efficiency, and the Earth's radiative energy budget.

Despite the fundamental importance of mixed-phase clouds, current knowledge of their formation and maintenance in the atmosphere is far from complete. This is due, to a large extent, to the lack of observations that can be used to accurately characterize the complex behaviors of various hydrometeors, their interplay with the dynamics, and their interactions with aerosols. The transformation from a fully liquid to a fully frozen cloud can follow a variety of non-linear paths. Accordingly, mixed-phase clouds are notoriously difficult to simulate in numerical weather prediction (NWP) and general circulation models (GCMs). Numerous studies have reported that a multitude of widely used GCMs and reanalysis datasets significantly underestimate the fraction of supercooled liquid water (SLW), compared to satellite-based estimates (e.g. Hu et al. 2010; Morrison et al. 2011; Huang et al. 2012a, b), particularly over the Southern Ocean (SO) where it directly contributes to the large simulated shortwave radiation biases (Bodas-Salcedo et al. 2014, 2016; Naud et al. 2014).

The prevalence of SLW over the SO suggested by satellite products is consistent with limited in-situ (Mossop et al. 1970; Chubb et al. 2013; Ahn et al. 2017) and ground-based observations (Kanitz et al. 2011). It has long been speculated that the scarcity of ice nucleating particles (INPs), such as dust, is largely responsible for the abundance of SLW in this remote region, far-removed from any natural or continental air source (Gras, 1995). Recent measurements of INP number concentrations (N_{INP}) during a ship campaign in the Australian sector of the SO found that the measured N_{INP} ranged from 0.38 to 4.6 m^{-3} at -20°C, a factor of 100 lower than those reported from historical surveys (McCluskey et al. 2018). Given such low INP concentrations, other physical mechanisms that may determine phase transformation in the SO clouds remain to be explored.

These recent findings have also supported a range of intense efforts towards improving the simulation of the SO clouds in climate models (e.g. Kay et al., 2016; Tan et al., 2016; Cesana and Storelvmo 2017). Using satellite estimates as an "observational constraint", attempts have been made to force the GCM parameterizations to increase the fraction of SLW (typically via specifying cloud phase as a function of temperature) in order to reduce the shortwave radiation biases (e.g. Kay et al. 2014; Lohmann and Neubauer 2018). Many of these exercises, however, use parameterizations with limited physical basis and therefore any ensuing feedback in the climate system is not well represented.

Satellite retrieval products, on the other hand, are limited by technical constraints. Huang et al. (2015) compared three cloud phase products derived from A-Train satellites (CALIPSO, MODIS, and a merged CloudSat-CALIPSO-MODIS product DARDAR-MASK), revealing large discrepancies in their phase classifications, even at cloud top. The accuracy of these products is even more questionable over the SO, given that the empirical relationships used in the retrieval algorithms are derived almost entirely from Northern Hemisphere datasets, themselves often limited (Ahn et al. 2018).

Existing in-situ cloud and aerosol observations over the SO, while limited, have been made available from several field campaigns spanning the past couple of decades. Major efforts include the Southern Ocean Cloud Experiment – SOCEX I and II (Boers et al. 1996, 1998), the first Aerosol Characterization Experiment – ACE 1 (Bates et al. 1998), the HIAPER Pole to Pole Observations – HIPPO (Wofsy et al. 2011; Chubb et al. 2013, 2016), a wintertime cloud microphysics field campaign near Tasmania of Australia (Ahn et al. 2017; Huang et al. 2015; 2017), and more recently the Southern Ocean Clouds, Radiation and Aerosol Transport Experimental Studies (SOCRATES) field campaign (McFarquhar et al. 2020). Many of the past field studies in this region have focused primarily on liquid/warm clouds and aerosols; only limited attention has been devoted to mixed-phase clouds, despite the fact that the Hallett-Mossop (H-M) ice multiplication mechanism (Hallett and Mossop 1974; Mossop and Hallett 1974; Mossop 1976) was originally discovered over the SO off the coast of Tasmania. Huang et al. (2017) presented a case study using in-situ cloud and aerosol data in conjunction with A-Train satellite observations over the open ocean near Tasmania, noting that ice multiplication (likely the H-M process) may be active in the open mesoscale cellular convection (MCC) clouds. These open MCCs, prevalent over the mid-latitude SO during the cold months (Muhlbauer et al. 2014; McCoy et al. 2017), are in direct contrast to the closed MCCs more commonly found over the high-latitude SO during the warm seasons. These findings complement the existing knowledge on the strong seasonal cycle of the cloud droplet number concentration (Boers et al. 1996, 1998) and cloud condensation nuclei (Ayers and Gras 1991) observed at/near Tasmania. It also suggests the need for a deeper understanding of the SO cloud systems and their natural variability.

In this study, we will expand the analysis in Huang et al. (2017) and Ahn et al. (2017) to employ the set of in-situ cloud and aerosol observations from 20 flights to characterize the wintertime cloud microphysical properties explicitly in the mixed-phase temperature regime (MPTR) over the mid-latitude SO. Ahn et al. (2017) focused on low-altitude (up to 3 km elevation) liquid clouds, even though a considerable fraction of the samples were taken at temperatures below freezing where ice was commonly encountered. Their selection of liquid cloud samples was found to frequently consist of intermittent drizzle with its intensity, droplet number concentration and effective radius being sensitive to the structure of the shallow convection (e.g. open vs. closed MCC). Our focus on MPTR in wintertime mid-latitude clouds will also complement the recent SOCRATES mission where the primarily target was the summertime boundary layer clouds in the cold sector of extratropical cyclones (McFarquhar et al. 2020).

2. Data and Methodology

2.1. Flight Overview

A comprehensive overview of the Tasmanian wintertime field experiment has been provided in Huang et al. (2017) and Ahn et al. (2017). In brief, these in-situ observations were made over 20 flights during Jun–Oct 2013–15 in the vicinity of Tasmania, Australia, with a lightly instrumented Cessna Conquest operated by Hydro Tasmania Ltd. As a key science objective of this field experiment was to examine the natural variability of the wintertime cloud microphysics over the mid-latitude SO, a variety of synoptic situations were sampled during these 20 flights. Due to the increasing risk of severe icing and lightning, heavy convective systems such as fronts and extratropical cyclones were largely avoided, limiting most of the samples to be within the lowest 5 km above sea level. Nevertheless, given the various meteorological conditions encountered, we can assume that the sampled clouds had formed and evolved in different environments including with respect to the vertical updrafts.

Twelve of the twenty flights were ‘research-only’ missions, which were dedicated to observing ‘pristine’ SO clouds where the sampled air masses were not subject to any upwind terrestrial influences according to the 72-hour back-trajectory analysis. Moreover, these flights were undertaken in close alignments with the A-Train satellite (Stephens et al., 2002) overpasses, allowing for near-concurrent observations of some common cloud targets. The remaining eight flights were comprised of ‘pristine’ segments of selected operational cloud-seeding flights, where on limited occasions the Cessna Conquest flew upwind of any seeding activity, off the coast to collect unperturbed samples for operational needs. Ahn et al. (2017) analyzed the liquid water effective radius and the droplet number concentration, finding no systematic biases between the 'research-only' missions and the upwind 'pristine' samples from the operational flights. As such, all 'pristine' samples collected from the twenty flights over the open ocean are used for the analysis of this study (Table 1).

2.2. Airborne Instrumentation

The airborne instruments, measurement capacity and their main limitations are summarized in Table 2. More detailed descriptions of the operating principles, the manner in which the data were processed and cloud parameters were determined, and limitations and uncertainty analysis can be found in Huang et al. (2017 and Appendices therein) and Ahn et al. (2017). In brief, particle size and number concentrations were measured and derived using the Droplet Measurement Technologies (DMT) Cloud, Aerosol and Precipitation Spectrometer probe (CAPS: Baumgardner et al., 2001), which consisted of a hot-wire liquid water sensor, a Cloud Aerosol Spectrometer (CAS), and a Cloud Imaging Probe (CIP). The CAS probe has a nominal size range of 0.6-50 μm in 30 size bins, and we separated its measurements into an aerosol data set and a cloud data set in this study (details provided later). The overall measurement uncertainties for particle concentrations and sizes are estimated to be ±20% for water droplets and ±30% for ice crystals (Baumgardner et al. 2017). The CIP probe measures larger particles (in less detail), nominally sizing particles between 50 μm and 1.55 mm in 62 size bins with 25 μm resolution. Its sizing accuracy is the same for droplets or ice crystals, with an average uncertainty of 25%. The concentration uncertainty estimated to be 20% (Baumgardner et al. 2017). All measurements were made and processed at 1 Hz temporal resolution, corresponding to a spatial scale of ~ 100 m at a typical aircraft true air speed of 100 m/s.

While aerosol composition and INP were not directly measured, we employ the DeMott et al. (2010, hereafter D10) parametrization to estimate the N_{INP} based on measured temperatures and CAS aerosol data (in clear air) with particle size down to ~0.6 μm, as per Huang et al. (2017). Among several INP schemes commonly used, the D10 estimates was shown to compare favorably with in-situ N_{INP} from primary nucleating particles (e.g. Grosvenor et al. 2012).

While much detailed information on data processing was provided in our earlier set of studies, two issues warrant some clarification, as these issues are relevant to the analyses of cloud phase identification and process interpretation in this study.

- CIP data processing

Particle images, sizes and concentrations measured by the CIP are processed and derived using the SODA2 program (Software for OAP Data Analysis, provided by A. Bansemer, National Center for Atmospheric Research /University Corporation for Atmospheric Research UCAR, 2013). A detailed description of SODA2 can be found in Frey et al. (2011). To minimize the sampling and sizing errors, several corrections were implemented with SODA2 including: (1) out of focus correction for particles showing a Poisson spot following Korolev et al. (2011); (2) 'center-in' correction (Heymsfield and Parrish, 1978) which is preferably used for quasi-symmetric or symmetric particles whose centers are located within the detector array; (3) shattered artifacts removed by rejecting particles with interarrival times of less than 10^{-4} s (Field et al. 2006). Moreover, poorly imaged particles with an area ratio (AR) below 0.1 or sizes outside of the measurement size range were also rejected. Given the large uncertainties in the probe's depth of field for small particle sizes in the first couple of bins (Baumgardner and Korolev, 1997), particles with D < 62.5 μm were not included in the analysis. For more reliable sizing, we have also used larger bin sizes by combining several bins of the original resolution to obtain sufficient particle counts across the measurement range.

- SEA WCM-2000 measurements

As discussed in Huang et al. (2017), SEA WCM-2000 is a relatively new probe and has not been as widely used as other hotwire instruments. This sensor measures liquid water content with two independent cylindrical hot-wire elements of different diameters, conventionally named WCM-021 (0.5 mm) and WCM-083 (2 mm), respectively. It also has a scooped 4-mm element WCM-156 for total water content ice plus liquid) measurements.

Following Korolev et al. (2003), we employed a generic approach for cloud phase partitioning. An "ice fraction" coefficient (μ) was calculated using the SEA WCM-2000 measurements. μ is defined as

$$\mu = \frac{W_{ice}}{W_{ice} + W_{liq}} \tag{1}$$

where *Wice* and *Wliq* are the ice and liquid water content calculated the same way as per Huang et al. (2017, Appendix C) following the method proposed in Korolev et al. (2003). The errors in calculating *Wice* and *Wliq* in mixed-phase clouds are related to uncertainties in the collection efficiencies of liquid drops and ice crystals by the sensors. When used in conjunction with the CAPS measurements, we expect the SEA data to provide reasonable and consistent results.

Qualitatively, cloud samples with $\mu < 0.3$ are defined as 'liquid', $0.3 \leq \mu \leq 0.9$ as 'mixed phase', and $\mu > 0.9$ as 'ice' in this study (Korolev et al. 2003; Field et al. 2004). Note that compared to previous studies (e.g. Korolev 2003; Ahn et al. 2017), we have chosen a more conservative threshold to distinguish 'liquid' and 'mixed phase' in order to reduce uncertainties associated with ambiguous samples. The threshold 0.3 was chosen after visually inspecting a large volume of concurrent CIP images where large ice particles could be detected with greater fidelity. We found that, at slightly supercooled temperatures where no ice was evident in the CIP, the WCM-156 element could sometimes record measurably higher water contents than those reported by the WCM-021 and WCM-083, particularly when large drizzle/rain drops were present. As such, the non-zero *Wice* calculated from these samples should be treated with greater caution. Changing the threshold from 0.3 to 0.2 and 0.4 led to the changes of the individual liquid and mixed phase fractions by ~ 30%, which is comparable to the measurement uncertainties of the CAPS probes.

2.3. A-Train cloud products

In the case studies presented in Section 4, several A-Train satellite cloud products are employed and compared with the in-situ observations. Two cloud phase products (Collection 6, Platnick et al., 2015) derived from the Moderate-Resolution Imaging Spectroradiometer (MODIS) onboard Aqua are examined: (1) the tri-spectral Infrared (IR)-based product (Baum et al., 2012) which reports cloud-top phase (hereafter CPI) using brightness temperature and emissivity ratios from three band pairs (8.5, 11, and 12 μm), and (2) the Cloud Phase Optical Property (CPOP), which is a daytime-only product derived from a combination of visible, shortwave IR, and IR channels (Marchant et al., 2016). In addition, the CALIPSO official level-2 Vertical Feature Mask (VFM, version 3.4) product (Hu et al., 2009) and a CloudSat-CALIPSO-MODIS merged product DARDAR-MASK version 1 (Delanoë and Hogan, 2010) are examined.

While in-situ validation studies of these phase products are rare, comparisons with the Polar Nephelometer measurements over the mid latitudes and the Arctic showed that the CALIPSO phase determination agrees well with the in-situ data for the homogeneous phase of midlatitude ice clouds, but is dominated by the cloud top phase when the clouds are vertically inhomogeneous (Cesana et al. 2016). It is also worth noting that the CALIPSO version-3 cloud phase product had underpinned the re-development of the MODIS C6 CPOP product (Platnick et al. 2015) and algorithm refinements of the CPI product (Baum et al. 2012). As a result, these two MODIS phase products no longer include a class for supercooled/mixed-phase clouds and instead these cases are presented as an ‘uncertain’ phase. Assuming the CALIPSO phase as “truth”, Platnick et al. (2015) reported that the MODIS C6 CPOP phase agrees with CALIPSO for 92% of the collocated CALIOP profiles when single-layer cloud scenes were examined. On the other hand, Baum et al. (2012) found that the CPI reported much higher percentages of uncertain phase, up to 40% (65%) more in the temperature range of -15℃ to -20℃ (-35℃ to -30℃) over ocean (land), when compared to CALIPSO single-layer phase.

3. Statistical Analysis for 20 Flights

Table 1 provides a brief overview the meteorological conditions, general thermodynamic characteristics (temperatures and winds), average cloud and aerosol characteristics sampled in the MPTR for all 20 flights. The synoptic settings ranged from pre-frontal, to post-frontal, to high-pressure and ridging conditions. Several types of MCC were also identified from visual inspections of the MODIS satellite true color images with a time window closest to the aircraft flight time. Nine of the twenty flights sampled the cloud fields that were classified as open MCC, while closed and no MCC conditions (typically characterized by solid cloud decks or a multi-layer coverage) also occurred (Figure 1 and Table 1).

In this study, a cloud sample was defined by a total water content (TWC) threshold of 0.01 g m^{-3} as measured by the SEA WCM-2000 as well as by the CAS probes. Given that the CAS measures particle size down to ∼0.6 μm, which includes the upper tail of the accumulation mode aerosols and giant nuclei, aerosol properties were also examined for samples taken in clear air. To avoid potential cloud contamination on the accuracy of aerosol sizing, clear air was defined when the CAS liquid water content LWC < 0.005 g m^{-3}, SEA WCM-2000 TWC < 0.005 g m^{-3}, and relatively humidity $< 80\%$.

Overall, 18,987s of cloud samples and 23,471s of aerosol samples were collected under the ‘pristine’ conditions in the MPTR down to -31℃ (Table 1 and Figure 2). While the smaller sample size from temperatures below -15℃ can partly be attributed to a sampling bias, it also reflects the shallow convective nature of these clouds as shown in the satellite-derived climatology (Huang et al. 2015). For all cloud samples within MPTR, liquid, mixed-phase, and ice cloud fractions were determined to be 39%, 44%, and 17%, respectively, using the μ method. Note that these statistics should not be compared directly to that reported in Ahn et al. (2017) as only low-altitude clouds detected below 3 km (including a considerable fraction of warm clouds) were examined in that study. The phase compositions varied significantly from flight to flight, with the liquid fraction varying from 2% to 90%, mixed-phase fraction from

9% to 95%, and ice fraction from 0% to 52%. These strong variabilities indicate the diverse physical nature of the sampled clouds, present under various meteorological conditions. Low number concentrations of small cloud particles (N_{CAS}) are also noted, with the flight-mean values varying from 5 to 70 cm^{-3}, consistent with the 'pristine' definition. The flight-mean N_{CAS} is negatively correlated with the number concentrations of large particles measured by the CIP (N_{CIP}) with a correlation coefficient of approximately 0.4, reflecting the growth of larger-size particles at the expense of small-size particles.

Using the in-situ data collected from a wide range of field campaigns, Korolev et al. (2003) reported a distinct pattern of the frequency of occurrence of the ice fraction μ, which has a U-shape distribution with maxima at $\mu = 0$ and $\mu = 1$ (an updated figure is provided in Korolev et al. 2017). They found that the occurrence of μ between 0.1 and 0.9 remained low and nearly constant in all temperature intervals. Here we performed the same analysis with our data and the results are shown in Figure 3. Overall, it is clear that the distribution of μ is not unimodal. While a semi U-shape distribution is identifiable, an increased fraction of μ in the range of 0.1-0.7 is notable in our data for all temperature intervals. A greater fraction of μ appears to fall in the range of 0.4-0.7 for the coldest temperatures sampled (-15 to -30℃), while the samples from the warmest temperatures (-5 to 0℃) feature a slightly higher fraction in 0.2-0.4. The μ distributions from samples in the mid-range temperatures (-15 to -5℃) appear flatter, with somewhat higher percentages in 0.7-0.9, which is suggestive of enhanced ice production (as will be discussed later). In order to rule out the possibility that the local peaks in the μ distributions are simply an instrument artefact, we also performed additional sensitivity tests by changing the value of the coefficient accounting for the ice residual effect on the liquid water sensor. The results show that these changes do not qualitatively change the characteristics of the distributions (not shown). Overall, the qualitative behaviors of μ suggest that some of these clouds were likely sampled in a transition state to glaciation. It is worth noting that the field data used in Korolev et al. (2003) were collected from both maritime and continental regions in the Northern Hemisphere mid- and high latitudes, whereas our data are representative of a pristine, maritime shallow convection in the SO mid-latitude storm track.

Using aircraft data from the summertime O_2/N_2 Ratio and CO_2 Airborne Southern Ocean (ORCAS) campaign round the Drake Passage and nearby regions, D'Alessandro et al. (2019) similarly provided the analysis of ice fraction but did not find scattered peak frequencies between 0.1 and 0.9. However, it should be noted that their ice fraction was derived from the

Cloud Droplet Probe and 2-Dimensional Cloud Probe, not hot-wire sensors with concave shapes as have been used in our study and in Korolev et al. (2003).

To explore any temperature dependence of the sampled cloud properties and N_{INP}, statistics of several measured and derived microphysical parameters as a function of temperature (with 3℃ bin intervals) are shown in Figure 4 (a-e). Analysis with smaller and larger bin sizes (1 and 5℃) are also performed but the characteristics of the results are qualitatively similar (not shown). Looking first at the statistics of small particle number concentrations (N_{CAS}) and the corresponding effective radius ($R_{32(CAS)}$), the statistics of both properties are largely stable at temperature from freezing to -15℃, with the average N_{CAS} varying in the range of ~ 10 to 25 cm^{-3} and $R_{32(CAS)}$ in the range of ~ 10 to 14 µm. The low N_{CAS}, once again, is consistent with Ahn et al. (2017), revealing the pristine nature of the sampled clouds. At colder temperatures (-15℃ to -30℃), both properties vary more strongly. Some relatively large N_{CAS} values (greater than 100 cm^{-3}) were recorded at temperatures below -15℃, which correspond to somewhat small ice fraction ($\mu < 0.6$). This suggests that, although shattered remnants in the CAS measurements cannot be ruled out, there remains a considerable fraction of liquid water within the clouds in these coldest observed temperatures.

Moving to the statistics of the number concentrations of large particles (N_{CIP}) and their effective radius ($R_{32(CIP)}$), not surprisingly, the largest values of N_{CIP} generally correspond to small $R_{32(CIP)}$ and low μ towards the warmer temperature end (-3 to 0℃), suggesting that the liquid dominated clouds typically contained drizzle. In the temperature range from -3℃ to -12℃, the N_{CIP} remain relatively stable with the mean concentration around 15 L^{-1} and the average $R_{32(CIP)}$ around 300 µm. The mean $R_{32(CIP)}$ is greatest from -18°C to -15°C (where it exceeds 400 µm), with notably lower N_{CIP} (several per liter). Particles recorded by the CIP images (not shown) indicate that ice crystals of various habits (e.g. aggregates, rimed crystals, capped columns, and dendrite) were common in this temperature range, along with several SLW drizzle-like drops. We will discuss these measurements in greater detail in the case studies presented in Section 4. At colder temperatures, the statistics of the CIP-derived parameters become more variable again, but only modest-size particles were recorded. It is worth noting that some of these samples were taken from mid-level altostratus and stratus detraining from the deeper cumulus.

In addition to the measured and derived cloud properties, the estimated N_{INP} from aerosol samples taken by the CAS in the 'pristine' airmass over the open water were also sorted by flight (Table 1) and segregated by temperature (Figure 4f). The D10 calculations have an uncertainty of around a factor of 10, as the aerosol composition is not considered in the algorithm. As such, primary nucleation is expected to form ice in concentrations within an order of magnitude of the estimated N_{INP} using this method. Our results show that the mean estimated N_{INP} increases from 10^{-3} L^{-1} at ~ -3℃ to 3 L^{-1} at -30℃. While these estimates are higher than recent shipborne observations (e.g. McCluskey et al. 2018), they are broadly consistent with historical surveys in this region (e.g. Atkinson et al. 2013). Potential seasonal variability and the fact that our aircraft measurements were taken much closer to land may account for some of the discrepancies. Nevertheless, our analysis shows that the N_{CIP} in heavily glaciated clouds (μ >0.9) is up to several orders of magnitude larger than the estimated N_{INP}, particularly within the H-M temperature range (-3 to -8℃) where the mean (maximum) N_{INP} is ~ 0.04 (0.15) L^{-1} while the estimated mean (maximum) N_{CIP} is ~ 9 (114) L^{-1}. In order to gain more confidence in the ice number concentrations estimated from the CIP, we further applied the 'water processing' correction available in SODA to calculate the number concentrations for potential water droplets (see Appendix D of Huang et al. 2017). We then subtracted the water droplet number concentrations from the N_{CIP} produced by the standard processing to obtain a more conservative estimate of the ice number concentrations. Using this method, the mean (maximum) N_{CIP} (ice) is estimated to be ~ 5 (50) L^{-1}. More specifically, in the temperature range of -15°C to -5°C, 25% of the estimated N_{CIP} (ice) is greater than 10 L^{-1}, approximately two orders of magnitude larger than the estimated N_{INP} in this temperature range. These results, together with the relatively small area ratios (Figure 4e), are indicative of the presence of graupel and/or pristine columnar features, suggesting a secondary production process. The temperature range is consistent with H-M laboratory studies, but other processes may be acting in the clouds.

The cloud particle size distributions (PSDs) measured by the CAS and CIP are shown in Figure 5, with the results sorted by cloud phase and temperature, respectively. The PSDs of all sampled clouds are dominated by a cloud mode peaked at ~13 μm. Such a peaked distribution is indicative of the presence of liquid water (Korolev et al. 2017). Little difference is found in the PSDs between the supercooled liquid clouds (i.e. liq in MPTR) and all liquid clouds, both of which feature a cloud mode with an extension to drizzle size. The distribution is rather smooth, consistent with coalescence. Ahn et al. (2017) noted that drizzle was common in these low-altitude liquid clouds. The PSDs of mixed-phase clouds also exhibit similar characteristics, but the number of medium size particles (62.5-200 μm) is slightly greater than the liquid counterparts. The PSDs of ice clouds appear to be more distinct, characterized by a clear decline in the number concentrations of medium size particles (62.5-200 μm) and higher number concentrations of larger particles (D >200 μm). It is noticeable that the increased concentrations of larger particles in the ice clouds do not correspond to a marked reduction of small particle concentrations. While this may indicate the presence of small ice, potential artifacts caused by shattering of the CAS probe cannot be ruled out.

Moving to the size spectra segregated by temperature, a distinct bimodal distribution is most notable for the coldest clouds sampled (-30 to -20℃), with a second mode forming at larger sizes (~400 μm). It is possible that the apparent increase in concentration for D<100 μm is associated with issues with sizing inaccuracies and compounding sample volume issues that inflate the concentration of these small particles (O'Shea et al. 2016). While the PSDs for the rest are largely similar, the colder samples (-20 to 0℃) appear to have higher concentrations of larger particles (D>200 μm) while the warm clouds have greater concentrations of medium-size particles (62.5-200 μm). The relatively large fraction of the medium-size range suggests, once again, the common presence of drizzles/raindrops in the warm clouds and high frequency of ice multiplication particles at temperatures down to -20℃.

4. Case Studies

In order to further investigate the microphysical characteristics of the shallow convective clouds typically sampled and the concurrent retrievals from various A-Train satellite products, observations from two flights are discussed in detail in this section.

4.1. Flight 20130707_125944

Figure 6a shows a MODIS 1.6-μm channel radiance image at ~ 04:25 UTC on July 7, 2013, overlaid by the aircraft and A-Train ground tracks. A large field of marine convective clouds (primarily open MCC), organized in sizes of several to tens of kilometers, was present in a prefrontal environment over the open ocean near Tasmania. Several characteristic cloud cells were sampled by the aircraft. Labels 'A-E' in Figure 6b-d indicate the approximate locations of the measured clouds, estimated based on the MODIS overpassing time, the aircraft flight time/location, as well as any drifting of the clouds corresponding to the northwesterly winds (Figure 7a). Given that the observed wind was 8-10 m/s, the potential drift of the cloud over a 20-min sampling period was up to ~ 0.15° longitude (12 km). Nevertheless, as the flight path was optimized to follow the drifting clouds (as shown by the meander of the aircraft track), we are confident that the sampling was made in very close alignment with the CloudSat/CALIPSO ground tracks.

Sampling at four levels was conducted through multiple cloud cells (Figure 6e-f and 8a). Level-1 (L1) was carried out with a southeastward heading at 1.5 km altitude and -4ºC, where two shallow clouds (‘A’ and ‘B’) were measured. The in-situ data indicate that cloud ‘A’ was primarily liquid, while cloud ‘B’ was occasionally in a mixed-phase state (μ was up to 0.3, Figure 8b-d) where particles that are fairly circular in shape (highlighted by red boxes in Figure 8e) were evident in the CIP images (Figure 8e). These were likely to be frozen raindrops, although some may simply be poorly imaged drops. There was some evidence of riming, but the almost spherical shape suggests that many of these frozen raindrops might have frozen recently. Moreover, some of Level-2 (L2) was headed northwards at an altitude of 2 km and -8ºC, where cloud ‘C’ was detected around 45ºS. The in-situ data indicate the presence of mixed phase (μ was up to 0.5, Figure 8b-d) with columns (pristine and hollow), needles, and SLW drizzle-like drops that are typically found in the H-M temperature zone (e.g. Hallett and Mossop, 1974; Huang et al., 2017; Grosvenor et al., 2012), together with some isolated rimed particles (Figure 8e). Given that these are the preferred growth ice habits close to water saturation, we infer that these particles have spent most of their lifetime at or near this altitude rather than being transported from above or below. Level-3 (L3) was run at 2.5 km altitude and -12ºC through a stronger convective cell with the top rising to ~4.5 km and -25ºC (‘D’). Graupel, irregular, and drizzle-like particles were recorded by the CIP with number concentration estimated to be ~ 20 L^{-1} (Figure 8e), while μ was up to 0.6. Their elongated or round shapes suggest that they originated as column or frozen raindrops. Along the uppermost sampling level (L4) where the aircraft penetrated a well identified large cell (‘E’) at 3.2 km altitude and -16ºC, in-situ data suggest mixed phase with μ in the range of 0.3-0.6. The CAS LWC was up to 0.8 g m^{-3}. Complex, mixed-habit ice particles (e.g. aggregates, heavily rimed crystals, and capped columns) were recorded by the CIP. These particles, which are typically formed when the particles have passed through several different growth regimes (e.g. riming and vapor deposition) during a cloud’s history (Korolev et al., 2000), suggest that they had been recirculated through multiple thermals or mixing processes.

The mean PSDs of all clouds sampled at the individual sampling levels are shown in Figure 9(a). As expected, a bimodal distribution is present for cloud samples taken from L2 to L4, with the large particle mode shifting towards larger sizes as the measured temperature (altitude) decreased (increased). This variation reflects the increased fraction of large ice particles from L1 to L4, consistent with our interpretation from Figure 8. The small particle mode exhibits a peak at ~13 μm regardless of the sampling levels, resembling the results from all clouds (Figure

5). Given the moderate μ values, this peaked distribution indicates the presence of SLW for all four levels.

Turning to the A-Train satellite phase products (Figure 6c-f), there appears to be a broad consistency between the MODIS CPI and CPOP products, although some major discrepancies are noted. The CPI product reports more ice and uncertain phase than the CPOP, particularly to the north of 45ºS. Vertical profiles of cloud phase retrievals from CALIPSO-VFM and DARDAR-MASK show that clouds to the north of 45ºS along the track are geometrically thin and/or multilayered, while those to the south become geometrically thicker. CALIOP detects the thin and multilayered clouds, but the lidar signals become fully attenuated through the thick layers, resulting in incomplete vertical profiles with the lower parts of the clouds undetected. As DARDAR-MASK incorporates observations from CloudSat cloud radar where available, the retrieved profiles contain the lower parts of the thick clouds, except in the lowest kilometer where the retrievals remain uncertain due to ground clutter effects (Marchand et al., 2008). Despite these limitations, it is evident that the CALIOP-VFM and DARDAR-MASK phase retrievals differ strongly throughout the vertical layers, even in the upper parts. The CALIOP-VFM retrievals are dominated by liquid down to -28ºC, whereas the DARDAR-MASK mainly reports ice all the way down to the freezing temperature, with intermittent mixed phase. Overall, the DARDAR-MASK phase in the upper parts of the clouds seems to be more consistent with the collocated MODIS-CPOP retrievals. The CALIOP-VFM does report some ice in the temperature range of -20ºC to -10ºC (45ºS-45.1ºS), but only horizontally oriented ice, which typically have stronger backscatter signals and smaller depolarization ratios.

4.2. Flight 20140903_124321

The cloud field in this case was observed along a leading edge of an anticyclonic ridge (Figure 10), characterized by relatively strong wind shear in the lower troposphere (Figure 7b). In order to measure a line of closely packed shallow clouds (mainly open MCC) residing primarily within the lowest 3 km, a different sampling strategy was adopted where a set of saw-tooth tracks was undertaken between approximately 150-m above sea level and 150-m above the observed shallow cloud tops along the CloudSat/CALIPSO ground tracks (Figure 10). During profiling, the aircraft passed through multiple cloud cells at temperatures from freezing to ~ -10ºC (see sounding in Figure 7b), generally consistent with the in-cloud temperatures reported in the satellite products (Figure 10e-f). Cloud samples at temperature colder than freezing are analyzed in Figure 11. For this case, labels ‘A-G’ in Figure 10 and 11 denote the groups of in-situ cloud samples. Note that only “groups” are examined in this case as the individual cloud cells cannot be reliably identified in the satellite images due to the complication of the overlying cirrus and the patchiness of these cells (1-10 km horizontal scales). Nevertheless, the consistency in the inferred cloud temperature and structure between the in-situ and the satellite products ensure that the same cloud regime was captured.

The in-situ data, once again, suggest that the observed clouds were primarily mixed phase (i.e. $0.3 < \mu < 0.6$), despite that shallow nature of these clouds. We note that groups 'C' and 'D' were heavily glaciated ($\mu > 0.9$). In the mixed-phase dominated group 'B', graupel-like particles are present in the CIP images at temperatures as warm as -4ºC, coexisting with drizzle-like drops (e.g. stripe 1 and 2 of cloud group 'B' in Figure 11e). In the heavily glaciated cloud group 'C', the images are overwhelmed by columns, needles, irregular, and, occasionally, small aggregates in the H-M temperature zone. Some of the columns were rimed, while some of them were greater than 1 mm in length. In another glaciated cloud 'D', a large quantity of smaller ice particles appearing as small capped columns and irregular shapes were captured by the CIP, with the size range of 150-250 μm and number concentrations of 40-50 L^{-1}. The maximum number concentrations are two to three orders of magnitude larger than the estimated N_{INP} (0.06 ± 0.02 L^{-1} for the whole flight over the sampling area and ~ 0.1 L^{-1} at -10ºC during sounding). Considering that the D10 INP parameterization has an uncertainty of a factor of 10, the observed maximum ice number concentrations were still one to two orders of magnitude greater than that of the estimated N_{INP}, suggesting that secondary ice production was once again active. The in-situ temperature of cloud 'D' was ~ -10ºC, which is colder than the H-M temperatures (-3ºC to -8ºC). It is therefore possible that the pristine columns produced from the H-M zone were transported to this cloud before being capped by the plates that are typically produced at temperatures of -10ºC to -15ºC. However, the relatively small size of these particles and the lack of larger graupel / rimed hydrometeors make it possible that other secondary ice production mechanisms (e.g. droplet shattering) might have played a role. Although detected at temperatures below 0℃, cloud groups 'A', 'E', and 'G' were primarily liquid phase. Overall, the in-situ observations from this case suggests the somewhat chaotic and spatially inhomogeneous nature of the secondary ice production processes.

Turning to the mean PSDs (Figure 9b), cloud "groups" containing large quantities of ice particles all exhibit a broader spectrum, with groups C and D characterized by a large particle mode peaked at 300 μm and 200 μm, respectively. The liquid dominated groups, on the other hand, all have presence of drizzle-size particles in the range of 62.5-100 μm. A cloud mode peaked at ~13 μm is, once again, evident for all sampling groups.

Satellite images reveal that, in addition to the extensive shallow convective clouds residing below 3 km (Figure 10e-f), some cirrus clouds forming at ~ 6-9 km were also present (Figure 10b-f). Therefore, the MODIS-CPI and CPOP are unable to determine the cloud properties below the high-elevation cirrus, returning only ice phase for the detected scenes. CALIPSO was able to pick up the multilayered cloud structure, although the lidar signals appear to have attenuated completely through the upper parts of the low-altitude clouds. As shown in Figure 10(e), virtually the entire upper layers of the low-altitude clouds are categorized as liquid phase in CALIPSO-VFM. The missing lower parts are retrieved in the DARDAR-MASK classification (Figure 10f). Unlike the CALIPSO-VFM, the DARDAR-MASK returns predominantly mixed phase along the cloud top with intermittent SLW. For much of the lower parts, DARDAR-MASK reports primarily ice down to the level of freezing. Such phase stratification is not uncommon in the DARDAR-MASK product (e.g. Huang et al., 2012b; Ceccaldi et al., 2013).

To summarize, in-situ data from the two cases show that the sampled shallow convective clouds were commonly present in a mixed phase at temperatures below freezing down to -12ºC, with ice particles exhibiting a variety of habits. While freezing of supercooled raindrops as the primary ice nucleation mechanism could be one hypothesis, ice multiplication (most likely rime splintering) was also observed to be active. The DARDAR-MASK and MODIS-CPI tend to report more glaciated clouds/cloud tops while CALIPSO-VFM and, to a lesser extent, MODIS-CPOP tend to produce more liquid phase.

5. Discussion and conclusions

In this study in-situ observations made by twenty flights during three Austral winters (June–October, 2013–2015) were analyzed to characterize the cloud microphysical properties and natural variability of the mid-latitude shallow convective clouds over the pristine Southern Ocean, with a focus on the mixed-phase temperature range (MPTR) from 0ºC to -31ºC. The principal findings are summarized as follows:

- Under the various synoptic conditions encountered, liquid, mixed-phase, and ice cloud fractions were observed to be 39%, 44%, and 17%, respectively. SLW was commonly detected in the MPTR.
- Alongside low droplet number concentrations, drizzle was commonly present in all liquid phase samples.

- Evidence suggests that freezing of supercooled raindrops likely form the primary ice nucleation mechanism, although this is not definitively clear.
- Ice particles of various habits were observed in mature/maturing convective clouds (with colder cloud tops), suggesting the operation of different particle growth regimes.
- Increased ice concentrations well in excess of that expected from primary ice nucleation signaled the operation of secondary ice production.
- High spatiotemporal inhomogeneity was found in secondary ice cloud segments, suggesting the chaotic and turbulent nature of this process.
- Large discrepancies are found in various satellite cloud phase products (both active and passive), with mixed phase cloud being a major challenge.

Results from this study allow for further comparisons with findings from other geographical regions. Using aircraft data from fourteen flights over the tropics and across the Northern Hemisphere, Costa et al. (2017) found that the observed cloud particles in the MPTR could be classified into four types: (a) mostly liquid with many small liquid droplets (D < 50 μm), (b) coexistence clouds with a high concentration of small particles (D < 50 μm) that can be liquid or frozen, (c) high concentration of small ice particles that might have emerged as a result of secondary ice production, and (d) fully glaciated Wegener-Bergeron-Findeisen (WBF) clouds, although those flights did not specifically target shallow convection only. While the CAS probe used in our study did not have the polarization capacity to distinguish the phase for small particles, our in-situ data in conjunction with the μ analysis suggest that type (a) and (b) clouds are rare in our observations; in contrast, the liquid-dominated clouds ($\mu < 0.1$) we observed commonly feature a coexistence of cloud droplets (D < 50 μm) and drizzle/rain drops (D > 62.5 μm). Approximately 60% of our liquid-dominated samples contain $N_{CIP} > 1$ L^{-1} and virtually all liquid-dominated samples that contain $N_{CIP} > 1$ L^{-1} also contain $N_{CAS} > 1$ cm^{-3}. Type (c) cloud is commonplace in the temperature range from -3℃ to ~ -12℃, while type (d) is relatively rare in our data, presumably due to the shallow, turbulent nature of the sampled clouds.

The common presence of drizzle and mixed phase clouds is intriguing. Given the limited vertical extent of these clouds, it is unlikely that the vertical updrafts therein could commonly exceed the strength required for reaching saturation with respect to liquid water (Korolev et al. 2007, 2017). Therefore, the WBF processes where ice particles grow at the expense of cloud droplets and possibly water vapor were likely to be active. On the other hand, in order to maintain/repeat the formation of mixed phase, sufficiently large updrafts that allow for water supersaturation would be a prerequisite, as well as frequent (re)supplying of condensate. In the absence of deep convection, these conditions only seem achievable via turbulent motions (especially shear-driven turbulence), as proposed in previous studies (Korolev and Field 2008; Hill et al. 2014; Field et al. 2014; Furtado et al. 2016). Field et al. (2004) suggested that observations of embedded liquid water regions with horizontal extents as short as 100 m may be the result of turbulent motions leading to the intermittent production of liquid water. Indeed, the lower-atmospheric wind shear as shown in our case studies as well as the long-term climatology derived from Macquarie Island soundings (Hande et al. 2012) suggest that turbulence prone conditions may not be uncommon over the mid-latitude SO. A shear-dominated environment further limits the convective growth of clouds.

Our observations also show that smaller ice particles with columnar features were detected in number concentrations up to two to three orders of magnitude larger than the estimated N_{INP} (noting that the our estimated N_{INP} might be biased high by a factor of 10 or more). These particles were primarily observed in the temperature range of -3ºC to -8ºC but could also be found at colder temperatures down to -12ºC. Graupel, rimed and drizzle-like particles were also often detected, alongside abundant supercooled cloud drops. The evidence therefore suggests that necessary conditions for H-M secondary ice mechanism were met, although other ice multiplication mechanisms such as droplet-shattering upon freezing might also be present. Given the shallow nature of these clouds, it is possible that multiple, successive thermals are necessary to produce the observed high ice number concentrations. Accurately representing these processes in global models, while necessary, is likely a challenge. A recent study by Atlas et al. (2020) has shown that even the Large Eddy Simulation (LES) has limited skills in reproducing the H-M ice multiplication in SO clouds (Altas et al. 2020).

It is, however, clear that the warm-rain and secondary ice processes are intimately linked. The H-M process requires cloud drops of certain sizes (appropriate numbers of droplets smaller than 12 μm and greater than 25 μm) and is accelerated by the presence of freezing drizzle/rain to form instant rimers (Phillips et al., 2001). Our observations provide some evidence of frozen drizzle-sized drops, with varying degree of riming, at temperatures as warm as -4 ºC. We note that similar features are also present in other flights under comparable conditions (not shown). This appears consistent with the majority of the first ice forming as freezing drizzle as reported in previous studies (e.g. Huang et al. 2008; Taylor et al. 2016). Indeed, primary ice nucleation via immersion freezing has been suggested to be the dominant ice nucleation mechanism in mixed-phase clouds (Ansmann et al., 2008; De Boer et al., 2011; Westbrook and Illingworth, 2011). We note that this does not preclude an 'ice seeding' scenario where ice particles produced in existing mixed-phase or glaciated clouds are transported by the outflows and become a seeder to the neighboring supercooled clouds. However, at least in our case 20130707_125944, no mixed-phase or ice clouds were notable immediately upwind in the vicinity of cloud "B" where possible frozen raindrops were identified.

The marked inconsistencies between the various satellite cloud phase products is a concerning point. The CALIPSO-VFM product reports predominantly liquid phase in the upper parts of the shallow convective clouds, while the lower parts are often under-detected. The DARDAR-MASK returns primarily mixed phase with intermittent SLW in the upper parts and ice below until the temperature reaches the freezing point. Based on the case studies, we infer that the space-based lidar is not able to identify the occurrence of mixed-phase clouds, especially when secondary ice particles are not necessarily produced at cloud tops. Our findings are also consistent with a recent study by Mace et al. (2020), where it was demonstrated that the original CALIPSO phase statistics has a severe low bias in the mixed-phase cloud occurrence over the mid-latitude SO, particularly during winter.

Our findings further suggest that simple thermodynamic arguments that have been commonly used in current modelling frameworks (e.g. Kay et al., 2016; Tan et al., 2016) cannot explain the processes involved in the production of the ice in supercooled clouds over the SO. Our analysis provides a statistical overview of typical microphysical properties observed in the MPTR having characteristics suggesting ice production processes in shallow convective clouds, but when and where these processes take place with respect to the cloud lifetime remains unclear. Given the rapid rate at which changes can occur, observing the evolution of these dynamic and turbulent systems is particularly challenging and hence not within the scope of this study. The lack of accurate in-situ measurements of simultaneous ice (including small ice), droplets, INPs and aerosol concentrations, as well as vertical velocity is another major limiting factor. Our study therefore should be seen as an incentive for further investigations into the ice forming processes in supercooled clouds over the SO, as well as their representation in global models and in satellite products.

Acknowledgements and Data Availability Statement:

This work is supported by an Australian Research Council discovery grant DP190101362 and CE170100023. The research flights were undertaken in cooperation with Hydro Tasmania. We thank the cloud seeding team from Hydro Tasmania for their consistent assistance with those

research flights. MODIS data were obtained from the NASA Level 1 and Atmosphere Archive and Distribution System (LAADS) Distributed Active Archive Center (DAAC): https://ladsweb.modaps.eosdis.nasa.gov/. CALIPSO data were obtained from the NASA the Atmospheric Science Data Center (ASDC): https://asdc.larc.nasa.gov/. DARDAR-MSAK data were obtained from the ICARE Thematic Center: https://www.icare.univ-lille.fr/. The aircraft data from the 20 flights can be accessed at: https://figshare.com/s/feb4d94d5be0ec502ee0.

References:

Ahn, E., Y. Huang, T. H. Chubb, D. Baumgardner, P. Isaac, M. de Hoog, S. T. Siems, M. J. Manton (2017): In situ observations of wintertime low-altitude clouds over the Southern Ocean. *Q. J. R. Meteorol. Soc*, **143**(704), 1381–1394. https://doi.org/10.1002/qj.3011.

Ahn, E., Y. Huang, S. T. Siems, M. J. Manton (2018): A comparison of cloud microphysical properties derived from MODIS and CALIPSO with in situ measurements over the wintertime Southern Ocean. *J. Geophys. Res. Atmos.*, **123**, 11,120–11,140. https://doi.org/10.1029/2018JD028535

Ansmann, A., and Coauthors (2008): Influence of Saharan dust on cloud glaciation in southern Morocco during the Saharan Mineral Dust Experiment, *J. Geophys. Res.*, **113**, D04210, doi:10.1029/2007JD008785.

Atkinson, J. D., B. J. Murray, M. T. Woodhouse, T. F. Whale, K. J. Baustian, K. S. Carslaw, S. Dobbie, D. O'Sullivan, and T. L. Malkin (2013): The importance of feldspar for ice nucleation bymineral dust in mixed-phase clouds, *Nature,* **498**, 355–358.

Atlas, R. L., C. S. Bretherton, P. N. Blossey, A. Gettelman, C. Bardeen, P. Lin, and Y. Ming (2020): How well do large-eddy simulations and global climate models represent observed boundary layer structures and low clouds over the summertime Southern Ocean? *J. Adv. Model. Earth Syst.*, **12**, e2020MS002205. https://doi.org/10.1029/2020MS002205.

Ayers, G. P., Cainey, J. M. (2007): The CLAW hypothesis: A review of the major developments. *Environ. Chem*. **4**: 366–374. https://doi.org/10.1071/EN07080.

Bates, T. S., B. J. Huebert, J. L. Gras, F. B. Griffiths, and P. A. Durkee (1998): International Global Atmospheric Chemistry (IGAC) Project's First Aerosol Characterization Experiment (ACE 1): Overview. *J. Geophys. Res. Atmos.*, **103**, 16297–16318, https://doi.org/10.1029/97JD03741.

Baum, B. A., W. P. Menzel, R. A. Frey, D. C. Tobin, R. E. Holz, S. A. Ackerman, A. K. Heidinger, and P. Yang (2012): MODIS cloud-top property refinements for Collection 6. *J. Appl. Meteor. Climatol.*, **51**, 1145–1163, doi:10.1175/JAMC-D-11-0203.1.

Baumgardner, D., and Korolev, A. (1997): Airspeed corrections for Optical Array Probe Sample Volume, *J. Atmos. Oceanic Technol.*, **14**, 1224–1229.

Baumgardner, D., H. Jonsson, W. Dawson, D. O'Connor, R. Newton (2001): The cloud, aerosol and precipitation spectrometer: A new instrument for cloud investigations, *Atmos. Res*. 59–60: 251–264.

Baumgardner, D., S. J. Abel, D. Axisa, R. Cotton, J. Crosier, P. Field, C. Gurganus, A. Haymsfield, A. Korolev, M. Kramer, P. Lawson, G. McFarquhar, Z. Ulanowski, J. UM (2017): Cloud ice properties: in situ measurement challenges. *Meteorol. Monogr*. **58**, Chapter 9. https://doi.org/10.1175/AMSMONOGRAPHS-D-16-0011.1.

Biter, C. J., J. E. Dye, D. Huffman, and W. D. King (1987): The dropsize response of the CSIRO liquid water probe, *J. Atmos. Oceanic Technol.*, **4**, 359–367, doi:10.1175/1520-0426(1987)004,0359:TDSROT.2.0.CO;2.

Boers, R., J. B. Jensen, P. B. Krummel, H. Gerber (1996): Microphysical and short-wave radiative structure of wintertime stratocumulus clouds over the Southern Ocean. *Q. J. R. Meteorol. Soc*. **122**: 1307–1339. https://doi.org/10.1002/qj.49712253405.

Boers, R., J. B. Jensen, P. B. Krummel (1998): Microphysical and radiative structure of marine stratocumulus clouds over the Southern Ocean: Summer results and seasonal differences. *Q. J. R. Meteorol. Soc*. **124**: 151–168. https://doi.org/10.1002/qj.49712454507.

Cesana, G., and T. Storelvmo (2017): Improving climate projections by understanding how cloud phase affects radiation, *J. Geophys. Res. Atmos.*, **122**, 4594-4599, doi:10.1002/2017JD026927.

Chubb, T. H., J. B. Jensen, S. T. Siems, and M. J. Manton (2013), In situ observations of supercooled liquid clouds over the Southern Ocean during the HIAPER Pole-to-Pole Observation campaigns, *Geophys. Res. Lett*. **40**: 5280–5285. https://doi.org/10.1002/grl.50986.

Chubb, T., Y. Huang, J. Jensen, T. Campos, S. Siems, and M. Manton (2016): Observations of high droplet number concentrations in Southern Ocean boundary layer clouds, *Atmos. Chem. Phys.*, **16**, 971–987, https://doi.org/10.5194/acp-16-971-2016.

Cober, S. G., G. A. Isaac, A. V. Korolev, and J. W. Strapp (2001): Assessing cloud phase conditions, *J. Appl. Meteor.*, **40**, 1967–1983, doi:10.1175/1520-0450(2001)040,1967:ACPC.2.0.CO;2.

Costa, A., J. Meyer, A. Afchine, A. Luebke, G. Günther, J. R. Dorsey, M. W. Gallagher, A. Ehrlich, M. Wendisch, D. Baumgardner, H. Wex, and M. Krämer (2017): Classification of

Arctic, midlatitude and tropical clouds in the mixed-phase temperature regime, *Atmos. Chem. Phys.*, **17**, 12219–12238, https://doi.org/10.5194/acp-17-12219-2017.

D'Alessandro, J. J., M. Diao, C. Wu, X. Liu, J. B. Jensen, B. B. Stephens (2019): Cloud phase and relative humidity distributions over the Southern Ocean in Austral summer based on in situ observations and CAM5 simulations. *J. Clim.*, **32**, 2781–2805, doi: 10.1175/JCLI-D-18-0232.1.

de Boer, G., H. Morrison, M. D. Shupe, and R. Hildner (2011): Evidence of liquid dependent ice nucleation in high-latitude stratiform clouds from surface remote sensors, *Geophys. Res. Lett.*, **38**, L01803, doi:10.1029/2010GL046016.

Delanoë, J., and R. J. Hogan (2010): Combined CloudSat-CALIPSO-MODIS retrievals of the properties of ice clouds, *J. Geophys. Res.*, **115**, D00H29, doi:10.1029/2009JD012346.

DeMott, P. J., A. J. Prenni, X. Liu, S. M. Kreidenweis, M.D. Petters, C. H. Twohy, M. S. Richardson, T. Eidhammer, D. C. Rogers (2010): Predicting global atmospheric ice nuclei distributions and their impacts on climate. *Proc. Natl. Acad. Sci*. U.S.A. **107**: 11217–11222.

Field, P. R., R. J. Hogan, P. R. A. Brown, A. J. Illingworth, T. W. Choularton, P. H. Kaye, E. Hirst, R. Greenaway (2004): Simultaneous radar and aircraft observations of mixed-phase cloud at the 100-m scale. *Q. J. R. Meteorol. Soc.* **130**: 1877–1904.

Field, P. R., A. J. Heymsfield, A. Bansemer (2006): Shattering and particle interarrival times measured by optical array probes in ice clouds, *J. Atmos. Oceanic Technol*. **23**: 1357–1371. https://doi.org/10.1175/JTECH1922.1.

Field, P. R., A. A. Hill, K. Furtado, and A. Korolev (2014): Mixed-phase clouds in a turbulent environment. Part 2: Analytic treatment. *Quart. J. Roy. Meteor. Soc*., **140**, 870–880. doi:10.1002/qj.2175.

Frey, W. (2011): Airborne in situ measurements of ice particles in the tropical tropopause layer, Ph.D. thesis, Johannes Gutenberg-Universität.

Furtado, K., P. R. Field, I. A. Boutle, C. J. Morcretteand, J. M. Wilkinson (2016): A physically based subgrid parameterization for the production and maintenance of mixed-phase clouds in a general circulation model. *J. Atmos. Sci.*, **73**: 279–291. doi: 10.1175/JAS-D-15-0021.1.

Gras, J. L. (1995), CN, CCN and particle size in Southern Ocean air at Cape Grim, *Atmos. Res.*, **35**, 233–251, doi:10.1016/0169-8095(94)00021-5.

Grosvenor, D. P., T. W. Choularton, T. Lachlan-Cope, M. W. Gallagher, J. Crosier, K. N. Bower, R. S. Ladkin, J. R. Dorsey (2012): In-situ aircraft observations of ice concentrations within clouds over the Antarctic Peninsula and Larsen Ice Shelf, *Atmos. Chem. Phys*. **12**: 11275–11294. https://doi.org/10.5194/acp-12-11275-2012.

Hallett, J., and Mossop, S (1974): Production of secondary ice crystals during the riming process, *Nature*, **249**: 26–28.

Hande, L. B., S. T. Siems, M. J. Manton, and D. Belusic (2012), Observations of wind shear over the Southern Ocean, *J. Geophys. Res. Atmos.*, **117**, D12206, doi:10.1029/2012JD017488.

Heymsfield, A. J., J. L. Parrish (1978): A computational technique for increasing the effective sampling volume of the PMS two-dimensional particle size spectrometer. *J. Appl. Meteorol*. **17**: 1566–1572.

Hill, A. A., P. R. Field, K. Furtado, A. Korolev, and B. J. Shipway (2014): Mixed-phase clouds in a turbulent environment. Part 1: Large-eddy simulation experiments. *Quart. J. Roy. Meteor. Soc.*, **140**, 855–869, doi:10.1002/qj.2177.

Hu, Y., and Coauthors (2009): CALIPSO/CALIOP cloud phase discrimination algorithm. *J. Atmos. Oceanic Technol.*, **26**, 2293–2309, doi:10.1175/2009JTECHA1280.1.

Hu, Y., S. Rodier, K. Xu, W. Sun, J. Huang, B. Lin, P. Zhai, and D. Josset (2010), Occurrence, liquid water content, and fraction of supercooled water clouds from combined CALIOP/IIR/MODIS measurements, *J. Geophys. Res.*, **115**, D00H34, doi:10.1029/2009JD012384.

Huang, Y., S. T. Siems, M. J. Manton, L. B. Hande, and J. M. Haynes. (2012a), The structure of low-altitude clouds over the Southern Ocean as seen by CloudSat, *J. Clim.*, **25**, 2535–2546, doi:10.1175/JCLI-D-11-00131.1.

Huang, Y., S. T. Siems, M. J. Manton, A. Protat, and J. Delanoë (2012b), A study on the low- altitude clouds over the Southern Ocean using the DARDAR- MASK. *J. Geophys. Res. Atmos.*, **117**, D18204, https://doi.org/10.1029/2012JD017800.

Huang, Y., A. Protat, S. T. Siems, and M. J. Manton (2015), A-train observations of maritime midlatitude storm-track cloud systems: comparing the Southern Ocean against the North Atlantic. *J. Clim.*, **28**(5), 1920–1939. https://doi.org/10.1175/JCLI-D-14-00169.1.

Huang, Y., T. H. Chubb, D. Baumgardner, M. de Hoog, S. T. Siems, and M. J. Manton (2017): Evidence for secondary ice production in Southern Ocean open cellular convection. *Q. J. R. Meteorol. Soc*, **143**, 1685–1703. https://doi.org/10.1002/qj.3041.

Huang, Y., A. M. Blyth, P. R. A. Brown, T. W. Choularton, P. Connolly, A. M. Gadian, H. Jones, J. Latham, Z. Cui, and K. Carslaw (2008): The development of ice in a cumulus cloud over southwest England, *New J. Phys.*, **10**, 105021, doi:10.1088/1367-2630/10/10/105021.

Kanitz, T., P. Seifert, A. Ansmann, R. Engelmann, D. Althausen, C. Casiccia, and E.G. Rohwer (2011), Contrasting the impact of aerosols at northern and southern midlatitudes on heterogeneous ice formation. *Geophy. Res. Lett*., **38**, 5. doi: L17802.

Kay, J. E., B. Medeiros, Y.-T. Hwang, A. Gettelman, J. Perket, and M. G. Flanner (2014): Processes controlling Southern Ocean shortwave climate feedbacks in CESM, *Geophys. Res. Lett.*, **41**, doi:10.1002/2013GL058315.

Kay, J. E., C. Wall, V. Yettella, B. Medeiros, C. Hannay, P. Caldwell, and C. Bitz (2016), Global climate impacts of fixing the Southern Ocean shortwave radiation bias in the Community Earth System Model (CESM). *J. Climate*, **29**, 4617-4636, doi:10.1175/JCLI-D-15-1231 0358.1.

Korolev, A. V., and Isaac, G. A. (2000): ‘Phase composition of stratiform clouds’. In Proceedings of 13th International Conference on Clouds and Precipitation, 14–18 August, 2000. Reno, NV, pp. 725–727.

Korolev, A., G. A. Isaac, S. G. Cober, J. W. Strapp, J. Hallett (2003): Microphysical characterization of mixed-phase clouds, *Q. J. R. Meteorol. Soc.* **129**: 39–65.

Korolev, A., and Field, P. R. (2008): The effect of dynamics on mixed-phase clouds: Theoretical considerations. *J. Atmos. Sci.*, **65**, 66–86, doi:10.1175/2007JAS2355.1.

Korolev, A. V., E. F. Emery, J. W. Strapp, S. G. Cober, G. A. Isaac, M Wasey, D. Marcotte (2011): Small ice particles in tropospheric clouds: Fact or artifact? Airborne icing instrumentation evaluation experiment. *Bull. Am. Meteorol. Soc*. **92**: 967–973. https://doi.org/10.1175/2010BAMS3141.1.

Korolev, A. V., E. F. Emery, and K. Creelman (2013): Modification and tests of particle probe tips to mitigate effects of ice shattering, *J. Atmos. Oceanic Technol*., **30**, 690–708.

Korolev, A. and P. R. Field (2015): Assessment of the performance of the inter-arrival time algorithm to identify ice shattering artifacts in cloud particle probe measurements, *Atmos. Meas. Tech.*, **8**, 761–777, https://doi.org/10.5194/amt-8-761-2015.

Korolev, A., G. McFarquhar, P. R. Field, C. Franklin, P. Lawson, Z. Wang, E. Williams, S. J. Abel, D. Axisa, S. Borrmann, J. Crosier, J. Fugal, M. Krämer, U. Lohmann, O. Schlenczek, M. Schnaiter, and M. Wendisch (2017): Mixed-Phase Clouds: Progress and Challenges, *Meteorol. Monogr.*, **58**, 5.1–5.50, https://doi.org/10.1175/amsmonographs-d-17-0001.1.

Lilie, L., E. Emery, J. W. Strapp, J. Emery (2005): 'A multiwire hot-wire device for measurement of icing severity, total water content, liquid water content, and droplet diameter'. In 43rd AIAA Aerospace Sciences Meeting and Exhibit, 10–13 January 2005. Aerospace Sciences Meetings. Reno, NV.

Lohmann, U. and Neubauer, D. (2018): The importance of mixed-phase and ice clouds for climate sensitivity in the global aerosol–climate model ECHAM6-HAM2, *Atmos. Chem. Phys.*, **18**, 8807–8828, https://doi.org/10.5194/acp-18-8807-2018.

Mace. G, S. Benson, Y. Hu (2020): On the frequency of occurrence of the ice phase in supercooled Southern Ocean low clouds derived from CALIPSO and CloudSa, *Geophy. Res. Lett.* **47**, e2020GL087554. doi: https://doi.org/10.1029/2020GL087554.

Marchand, R., G. G. Mace, T. Ackerman, and G. Stephens (2008): Hydrometeor detection using CloudSat - An Earth orbiting 94-GHz cloud radar, *J. Atmos. Oceanic Technol.*, **25**, 519–533, doi:10.1175/2007JTECHA1006.1.

Marchant, B., S. Platnick, K. Meyer, G. T. Arnold, and J. Riedi (2016): MODIS Collection 6 shortwave-derived cloud phase classification algorithm and comparisons with CALIOP. *Atmos. Meas. Tech.*, **9**, 1587–1599, doi:10.5194/amt-9-1587-2016.

McCoy, I. L., R. Wood, and J. K. Fletcher (2017): Identifying Meteorological Controls on Open and Closed Mesoscale Cellular Convection Associated with Marine Cold Air Outbreaks, *J. Geophys. Res.-Atmos.*, **122**, https://doi.org/10.1002/2017JD027031.

McFarquhar, G., C. Bretherton, R. Marchand, A. Protat, P. Demott, S. Alexander, et al. (2020): Observations of clouds, aerosols, precipitation, and surface radiation over the southern ocean: An overview of CAPRICORN, MARCUS, MICRE and SOCRATES, *Bulletin of the American Meteorological Studies*. doi: https://doi.org/10.1175/BAMS-D-20-0132.1.

Mossop, S. C., and Hallett J. (1974): Ice crystal concentration in cumulus clouds: Influence of the drop spectrum, *Science*, **186**: 632–634.

Muhlbauer, A., I. L. McCoy, R. Wood (2014): Climatology of stratocumulus cloud morphologies: Microphysical properties and radiative effects, *Atmos. Chem. Phys.* **14**: 6695–6716. https://doi.org/10.5194/acp-14-6695-2014.

Morrison, A. E., S. T. Siems, and M. J. Manton (2011): A cloud-top phase climatology of Southern Ocean clouds, *J. Clim.*, **24**, 2405–2418, doi:10.1175/2010JCLI3842.1.

McCluskey, C. S., T. C. J. Hill, R. S. Humphries, A. M. Rauker, A. M., S. Moreau, S., P. G. Strutton, S. D. Chambers, A. G. Williams, I. McRobert , J. Ward, M. D. Keywood, J. Harnwell, W. Ponsonby, Z.M. Loh , P. B. Krummel, A. Protat, S.M. Kreidenweis, and P. J. DeMott (2018): Observations of ice nucleating particles over Southern Ocean waters. *Geophy. Res. Lett.*, **45**, 11,989–11,997. https://doi.1294/org/10.1029/2018GL079981.

O'Shea, S. J., T. W. Choularton, G. Lloyd, J. Crosier, K. N. Bower, M. Gallagher, S. J. Abel, R. J. Cotton, P. R. A. Brown, J. P. Fugal, O. Schlenczek, S. Borrmann, and J. C. Pickering (2016): Airborne observations of the microphysical structure of two contrasting cirrus clouds. *J. Geophys. Res. Atmos.*, **121,** 13,510–13,536, doi:10.1002/2016JD025278.

Phillips, V. T. J., A. M. Blyth, P. R. A. Brown, T. W. Choularton, and J. Latham (2001): The glaciation of a cumulus cloud over New Mexico, *Q. J. Roy. Meteor. Soc.*, **127**, 1513–1534, doi:10.1002/qj.49712757503.

Platnick, S. and Coauthors (2015): MODIS Cloud Optical Properties: User Guide for the Collection 6 Level-2 MOD06/MYD06 product and associated level-3 datasets. NASA Goddard Space Flight Center, 140 pp. [Available online at http://modis-atmos.gsfc.nasa.gov/_docs/C6MOD06OPUserGuide.pdf.]

Steen, L. C. E., R. F. Ide, and J. F. Van Zante (2016): An assessment of the icing blade and the SEA multi-element sensor for liquid water content calibration of the NASA GRC Icing Research Tunnel. Eighth AIAA Atmospheric and Space Environments Conf., Washington, DC, AIAA, 2016-4051, doi: https://doi.org/10.2514/6.2016-4051.

Stephens, G. L., Vane, D. G., Boain, R. J., Mace, G. G., Sassen, K., Wang, Z., et al. (2002). The CloudSat mission and the A-train: A new dimension of space-based observations of clouds and precipitation, *Bulletin of the American Meteorological Society*, **83**, 1771–1790. https://doi.org/10.1175/BAMS-83-12-1771.

Strapp, J. W., and Coauthors (2003): Wind tunnel measurements of the response of hot-wire liquid water content instruments to large droplets, *J. Atmos. Oceanic Technol.*, **20**, 791–806, doi:10.1175/1520-0426(2003)020,0791:WTMOTR.2.0.CO;2.

Tan, I., T. Storelvmo, and M. D. Zelinka (2016): Observational constraints on mixed-phase clouds imply higher climate sensitivity, *Science*, **352**, 224-227. https://doi.org/10.1126/science.aad5300.

Taylor, J. W., T. W. Choularton, A. M. Blyth, Z. Liu, K.N. Bower, J. Crosier, M. W. Gallagher, P. I. Williams, J. R. Dorsey, M. J. Flynn, L. J. Bennett, Y. Huang, J. French, A., Korolev and P. R. A. Brown (2016): Observations of cloud microphysics and ice formation during COPE, *Atmos. Chem. Phys*., **16**, 799–826, doi:10.5194/acp-16-799-2016.

Westbrook, C. D., and Illingworth, A. J. (2013): The formation of ice in a long-lived supercooled layer cloud, *Q. J. R. Meteorol. Soc*.,**139** (677), 2209–2221, doi:10.1002/qj.2096.

Wofsy, S. C., the HIPPO Science Team, and Cooperating Modeling and Satellite Teams (2011): HIAPER Pole-to-Pole Observations (HIPPO): fine-grained, global-scale measurements of climatically important atmospheric gases and aerosols. *Phil. Trans. Roy. Soc.* A, **369**, 2073-2086, doi:10.1098/rsta.2010.0313.

Table Captions

Table 1 Summary of meteorological conditions, average cloud and aerosol microphysical properties for each of the 20 flights.

Table 2 Summary of in-situ instruments on board the Cessna Conquest aircraft.

Figure Captions

Figure 1. True colour images from MODIS aboard Aqua satellite providing an overview of the cloud fields sampled by the twelve research flights. Sampled areas for the individual flights are highlighted by the red ellipses.

Figure 2. Counts of samples collected by the 20 flights as a function of temperature with 3℃ bin intervals. (a) cloud samples. (b) aerosol samples.

Figure 3. Probability Density Function (PDF) of ice fraction (μ) for different temperature intervals within the MPTR for 'pristine' clouds sampled by the 20 flights of three consecutive winters.

Figure 4. Statistics of measured and derived cloud properties as a function of temperature. (a) CAS number concentration (N_{CAS}). (b) Effective radius derived from CAS measurements ($R_{32(CAS)}$). (c) CIP number concentration (N_{CIP}). (d) Effective radius derived from CIP measurements ($R_{32(CAS)}$). (e) Area Ratio (AR) derived from CIP measurements. (f) estimated N_{INP} using the D10 parameterization scheme. Mean values (red dots), median values (short lines) and quartiles are shown.

Figure 5. Composite of normalized particle size distributions (PSDs) measured by the CAS and CIP for different (a) cloud types and (b) temperature ranges. CAS measurements are indicated by dashed curves and CIP measurements are indicated by solid curves.

Figure 6. A-Train satellite images for Case 20130707_125944. (a) MODIS 1.6-µm radiance at ~ 04:25 UTC on July 7, 2013, overlaid by the A-Train (red) and flight (yellow) ground tracks, (b) the zoomed-in MODIS cloud-top temperature image overlaid by the A-Train and flight ground tracks, (c) same as (b) but for MODIS-CPI, (d) same as (b) but for MODIS-CPOP, (e) the CALIPSO-VFM cross-section overlaid with ECMWF temperature contours and flight altitudes (red), HOI indicates horizontal oriented ice, (f) same as (e) but for DARDAR-MASK cross-section. The green box in (a) indicates the sampled area. Labels 'A-

E' in (b-d) indicate the approximate positions of the measured clouds (see text for details). L1-L4 in (e-f) indicate the aircraft sampling levels.

Figure 7. Airborne soundings undertaken during the two flight cases near the sample areas. (a) Sounding from Case 20130707_125944 around 05UTC. (b) Sounding from Case 20140903_124321 around 05UTC. Temperature profiles are in red and dewpoint profiles are in blue. Wind data between 900 and 720 hPa in Case 20140903_124321 are missing.

Figure 8. Times series of the in-situ measurements for Case 20130707_125944. (a) Flight altitudes and ambient temperatures. (b) Ice fraction μ. (c) CAS mass and number concentrations. (d) CIP mass and number concentrations [mass concentrations of liquid water in blue (red) are calculated assuming all detected particles are liquid (ice)]. (e) Particle images recorded by the CIP (strip width 1.55 mm). Labels L1-L4 (A-E) correspond to L1-L4 (A-E) in Figure 6. The two red dashed lines in (b) indicate 'ice fraction' thresholds used to distinguish liquid, mixed phase, and ice cloud phase. The images highlighted by red boxes are examples of frozen rain drops that may have grown by vapor diffusion.

Figure 9. Same as Figure 5 but for (a) all cloud samples from levels L1-L4, respectively, from Case 20130707_125944, and (b) all cloud samples from groups A-G, respectively, from Case 20140903_124321. Labels L1 to L4 in (a) correspond to L1 to L4 in Figure 6. Labels A-G in (b) correspond to groups A-G in Figure 11.

Figure 10. Same as Figure 6 but for Case 20140903_124321.

Figure 11. Same as Figure 8 but for Case 20140903_124321. Labels 'A-G' denote the groups of in-situ cloud samples in this case.

Table 1 Summary of meteorological conditions, average cloud and aerosol microphysical properties for each of the 20 flights

Flight ID	Category	Synoptic Type	Wind Direction (º)	Cloud Type	In-cloud time in MPTR (sec)	*Temperature Range (ºC)	Liq (%)	MP (%)	Ice (%)	N_{CAS} (cm^{-3})	$R_{32(CAS)}$ (μm)	N_{CIP} (L^{-1})	$R_{32(CIP)}$ (μm)	AR_{CIP}	Cloud-free time in MPTR (sec)	N_{INP} (L^{-1})
20130614_133658	R	Low pressure to the east	145	Open MCC	348	-5.54 - -0.26 [-1.62]	88	12	0	33 (18)	8.9 (1.8)	4 (3)	59 (17)	0.60 (0.09)	1172	0.35 (0.36)
20130628_130139	R	Ridge	194	Open MCC	1006	-4.54 – 0 [-1.12]	66	34	0	21 (13)	13.5 (2.5)	41 (30)	98 (45)	0.58 (0.05)	897	0.05 (0.15)
20130702_101141	o	Near front (~ 120 km)	275	No MCC	1413	-12.35 – 0 [-6.28]	13	35	52	18. (10)	14.0 (2.1)	19 (29)	522 (215)	0.54 (0.07)	8	0.007 (0.002)
20130707_073753	o	Pre-frontal	320	Open MCC	249	-13.27 - -1.99 [-8.48]	20	64	16	18 (11)	14.7 (1.6)	41 (35)	261 (185)	0.52 (0.06)	353	0.61 (0.73)
20130707_125944	R	Pre-frontal	274	Open MCC	2163	-31.18 - -3.89 [-15.55]	60	40	0	70 (91)	12.9 (2.6)	11 (12)	375 (132)	0.53	570	0.94 (1.49)
20130723_130219	R	Ridge	183	Closed MCC	0	All above freezing	-	-	-	-	-	-	-	-	0	-
20130803_084439	o	Pre-frontal	261	No MCC	401	-9.87 - -8.82 [-9.31]	2	95	3	5 (2)	13.1 (0.8)	4 (1)	531 (86)	0.57 (0.03)	116	0.14 (0.03)
20130806_151347	R	Post-frontal	247	Open MCC	431	-13.62 - -2.73 [-6.22]	76	23	1	33 (20)	10.1 (2.2)	6 (10)	129 (102)	0.58 (0.09)	1013	0.21 (0.54)
20130815_122404	R	Ridge	302	Disorganized MCC	1522	-6.88 - -0.04 [-4.61)]	75	24	1	15 (12)	10.9 (2.9)	15 (22)	194 (176)	0.51 (0.08)	3768	0.19 (0.40)
20130907_122442	R	Post-frontal	257	Open MCC	1850	-10.88 - -0.57 [-6.28]	27	41	32	25 (24)	13.1 (2.2)	13 (9)	282 (146)	0.49 (0.09)	4486	0.18 (0.58)
20130921_113331	o	Near front (~ 400 km)	257	No MCC	206	-10.09 - -3.28 [-9.16]	90	9	1	30 (8)	8.1 (1.2)	0.2 (0.4)	53 (22)	0.55 (0.15)	266	0.15 (0.06)
20131011_074911	o	Near front (~ 50 km)	276	No MCC	1348	-15.19 - -0.04 [-9.20]	22	70	8	23 (10)	12.7 (2.0)	42 (46)	340 (240)	0.52 (0.06)	5	0.005 (0.001)
20131011_132432	R	Post-frontal	273	Disorganized MCC	979	-25.46 - -0.12 [-11.90]	52	30	18	17 (15)	10.5 (3.1)	6 (14)	342 (269)	0.50 (0.09)	1350	0.74 (0.81)
20140630_070840	o	Pre-frontal	259	Not identified	347	-10.46 - -8.46 [-9.55]	73	24	3	10 (9)	12.1 (2.2)	20 (28)	152 (169)	0.55 (0.06)	521	0.10 (0.02)
20140806_150804	o	Near front (~ 50 km)	264	No MCC	1236	-13.93 - -4.98 [-8.53]	23	38	39	28 (23)	12.0 (2.5)	N/A	N/A	N/A	257	0.33 (0.29)
20140903_124321	R	Ridge	224	Open MCC	516	-10.51 - -0.05 [-4.74]	44	41	15	19 (15)	13.1 (2.3)	24 (23)	157 (137)	0.55 (0.08)	2449	0.07 (0.16)
20140912_124317	R	South of high pressure	264	Open MCC	1159	-26.40 - -0.02 [-8.22]	41	32	27	13 (15)	12.5 (2.5)	32 (41)	153 (131)	0.56 (0.04)	1598	0.05 (0.27)
20150804_121910	o	Pre-frontal	279	No MCC	2669	-12.13 - -0.01 [-9.76]	14	59	28	35 (26)	12.2 (2.9)	19 (23)	275 (224)	0.55 (0.07)	622	0.11 (0.01)
20150830_130524	R	High pressure to the south	151	Open MCC	660	-5.01 – 0 [-1.04]	18	82	0	16 (14)	12.7 (2.9)	78 (42)	79 (28)	0.60 (0.03)	1147	0.28 (0.81)
20151001_123025	R	Post-frontal	260	Closed MCC	484	-19.16 - -0 [-10.98]	33	61	6	50 (32)	8.6 (2.8)	0.8 (1.5)	263 (241)	0.54 (0.12)	2873	0.38 (0.72)
Total					18987		39	44	17	29 (39)	12.3 (2.8)	19 (30)	277 (217)	0.54 (0.07)	23471	0.30

Cloud type: MCC (mesoscale cellular convection) Flight type: R (Research), O (Operational) N/A: probe did not function properly

Meteorological conditions/classifications are adopted from Ahn et al. (2017). Numbers in parentheses indicate mean values (column 7) or standard deviations (columns 11-15 and 17).

Table 2 Summary of in-situ instruments on board the Cessna Conquest aircraft

Airborne Instrumentation	Measurement capacity	Main limitations and uncertainties
Droplet Measurement Technologies (DMT) Cloud Aerosol and Precipitation Spectrometer (CAPS, Baumgardner et al. (2001))	(1) a hot-wire liquid water sensor measuring liquid water content from 0.001 to 3 g m^{-3}. (2) a single particle light scattering Cloud and Aerosol Spectrometer (CAS) measuring cloud and aerosol size in the range of 0.6–50 μm (3) an optical Cloud Imaging Probe (CIP-25) measuring cloud and precipitation particle in the range 50 μm to 1.55 mm	The CAS probe does not discriminate signals from ice particles and liquid droplets. This may result in an overestimation of measured droplet concentration and liquid water content in mixed-phase clouds (e.g., Korolev et al. 2013). The CAS was not equipped with anti-shattering tips so ice fragments cause by shattering may artificially enlarge the ice particle concentrations (Field et al. 2006; Korolev and Field, 2015). Similarly, the CIP probe was not equipped with the anti-shatter tips prior to 2015. The re-combined bin sizes used for CIP analysis are [62.5, 125.0, 175.0, 225.0, 275.0, 325.0, 400.0, 475.0, 550.0, 625.0, 700.0, 800.0, 900.0, 1000.0, 1200.0, 1400.0, 1600.0] μm.
Science Engineering Associates (SEA, Tolland CT, USA) WCM-2000 Multi-Element Water Content System (Lilie et al. 2005; Steen et al. 2016)	(1) one cylindrical hot-wire element (0.5 mm in diameter) measuring liquid water content (2) one cylindrical hot-wire element (2 mm in diameter) measuring liquid water content (3) one scooped 4-mm element measuring total water content (ice plus liquid)	This instrument is designed to minimize the issues that the older model hotwire probes have, i.e. decreased sensitivity for larger droplets (Biter et al., 1987; Strapp et al., 2003) and the response of the liquid water content sensor to ice crystals (Cober et al., 2001). Although Lilie et al. (2005) show wind tunnel measurements that suggest that the WCM-2000 does not roll off until much larger drop sizes than other hotwire instruments; it is very likely that the WCM-021 sensor will respond to ice crystals similar to the hotwire with the same dimension. This means that in mixed-phase clouds, the separation between liquid and solid phase may still be biased.
Meteolabor TP-3S (Meteolabor AG, Switzerland)	Ambient and dew-point temperatures	N/A

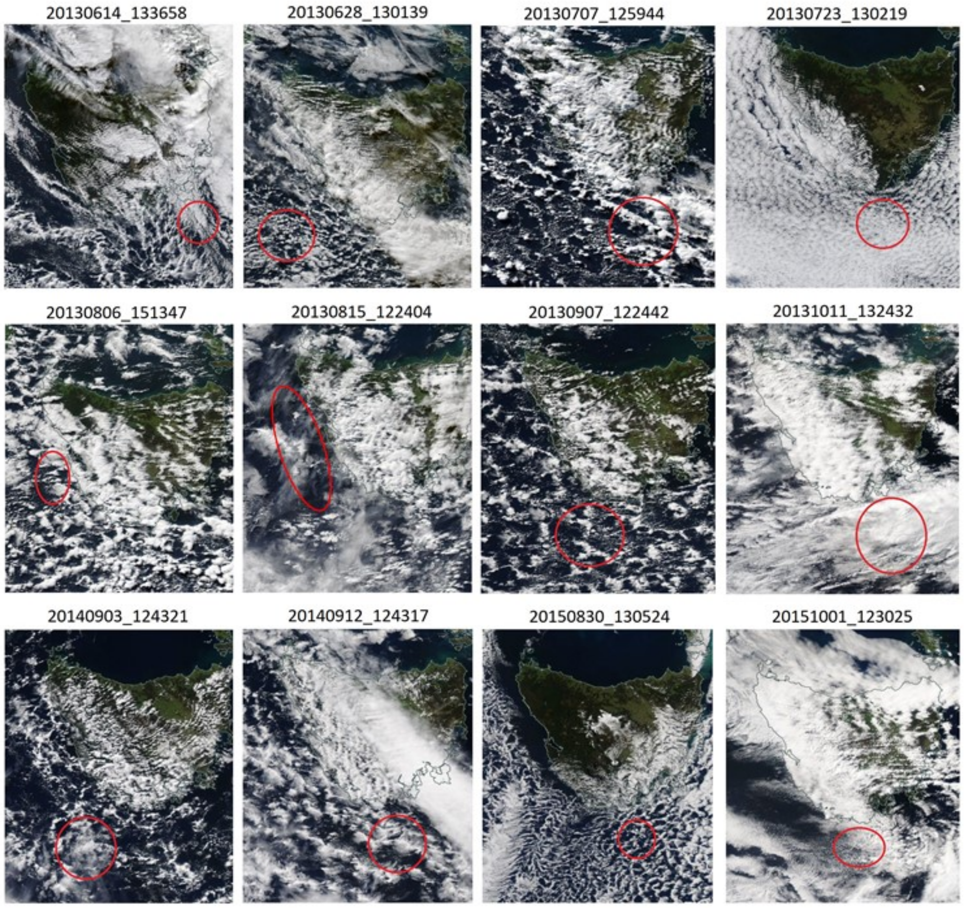
20130614_133658
20130628_130139
20130707_125944
20130723_130219
20130806_151347
20130815_122404
20130907_122442
20131011_132432
20140903_124321
20140912_124317
20150830_130524
20151001_123025

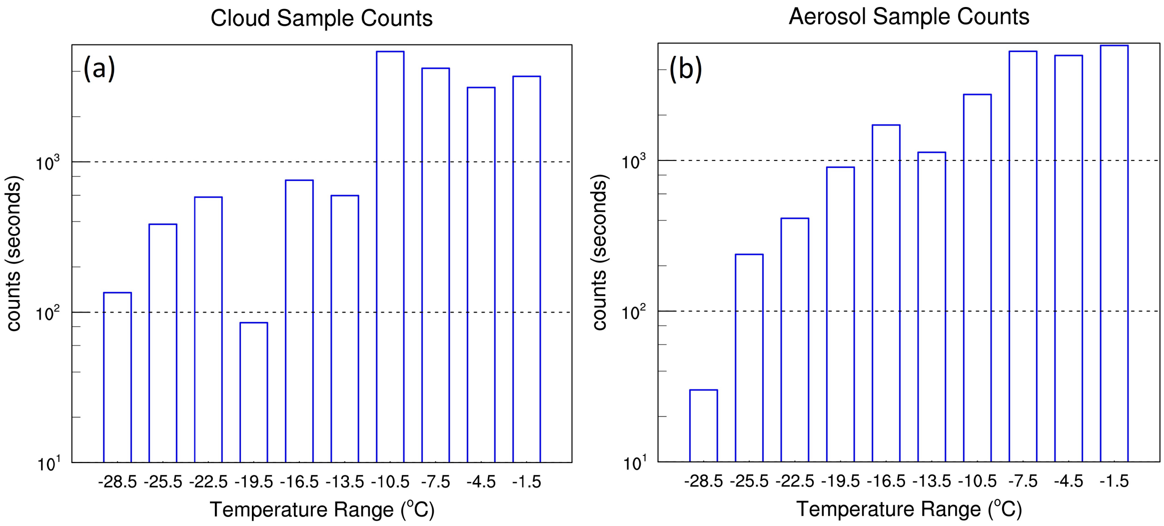
Cloud Sample Counts
(a)
counts (seconds)
10^1
10^2
10^3
-28.5
-25.5
-22.5
-19.5
-16.5
-13.5
-10.5
-7.5
-4.5
-1.5
Temperature Range (°C)
Aerosol Sample Counts
(b)
counts (seconds)
10^1
10^2
10^3
-28.5
-25.5
-22.5
-19.5
-16.5
-13.5
-10.5
-7.5
-4.5
-1.5
Temperature Range (°C)

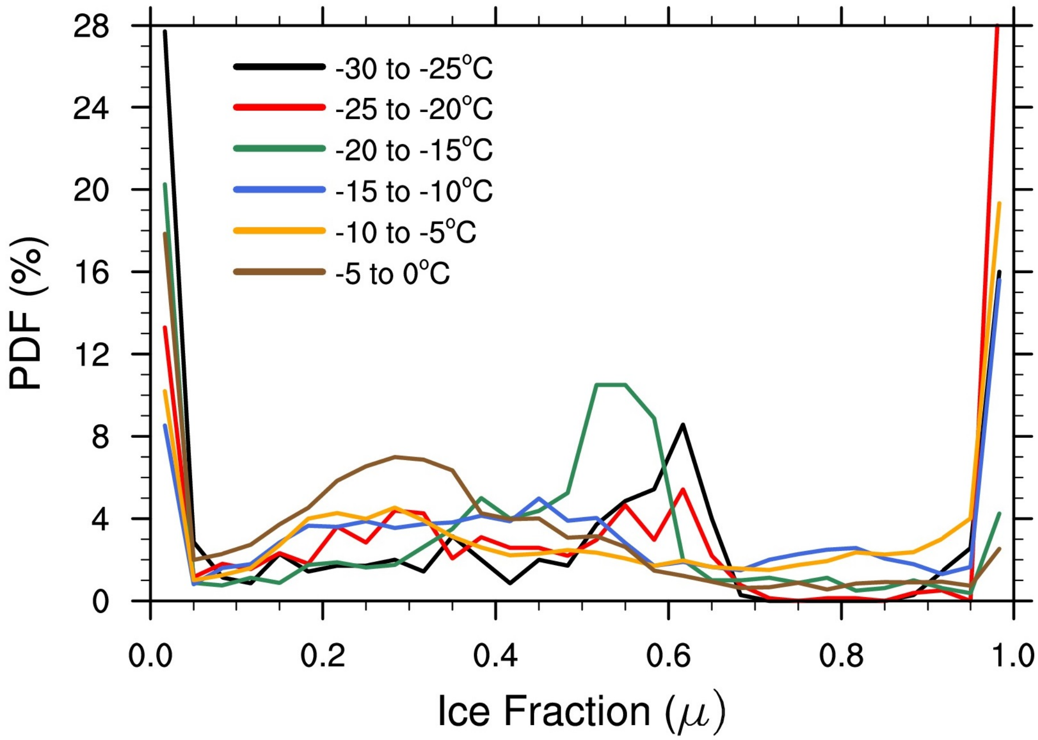
28
24
20
16
12
8
4
0
PDF (%)
0.0
0.2
0.4
0.6
0.8
1.0
Ice Fraction (μ)
-30 to -25°C
-25 to -20°C
-20 to -15°C
-15 to -10°C
-10 to -5°C
-5 to 0°C

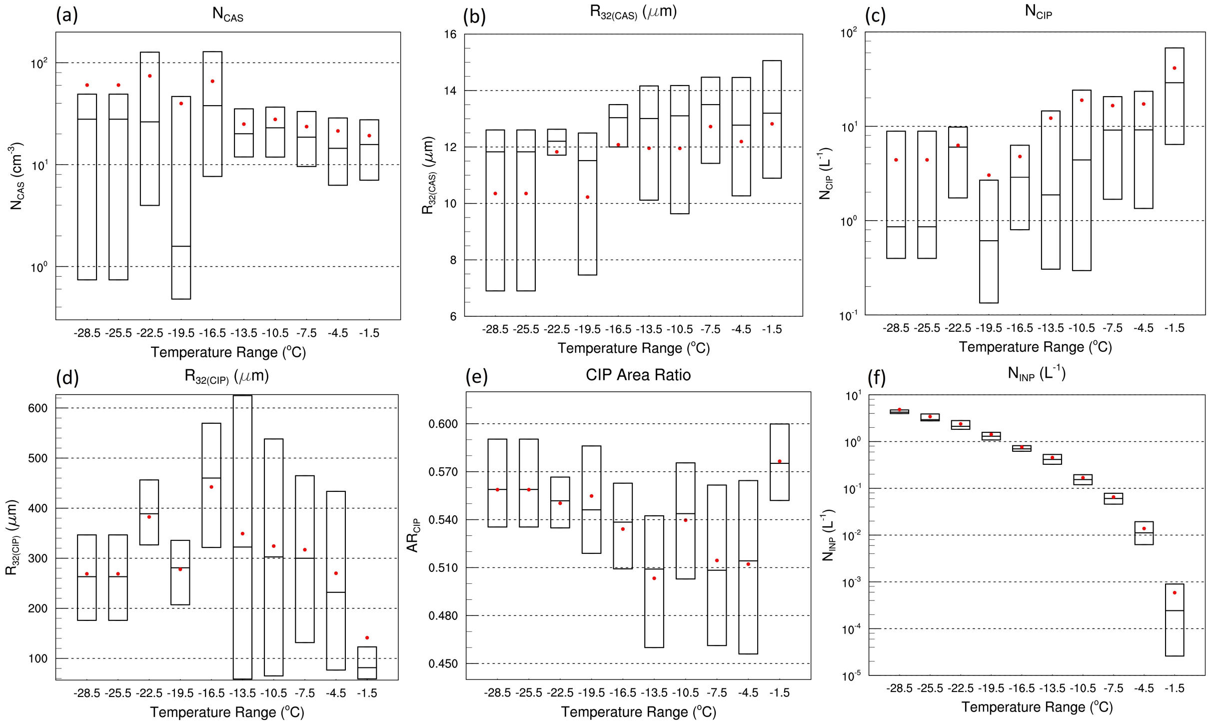
(a)
N_{CAS}
N_{CAS} (cm^{-3})
10^2
10^1
10^0
(b)
$R_{32(CAS)}$ (μm)
$R_{32(CAS)}$ (μm)
16
14
12
10
8
6
(c)
N_{CIP}
N_{CIP} (L^{-1})
10^2
10^1
10^0
10^{-1}
(d)
$R_{32(CIP)}$ (μm)
$R_{32(CIP)}$ (μm)
600
500
400
300
200
100
(e)
CIP Area Ratio
AR_{CIP}
0.600
0.570
0.540
0.510
0.480
0.450
(f)
N_{INP} (L^{-1})
N_{INP} (L^{-1})
10^1
10^0
10^{-1}
10^{-2}
10^{-3}
10^{-4}
10^{-5}
-28.5 -25.5 -22.5 -19.5 -16.5 -13.5 -10.5 -7.5 -4.5 -1.5
Temperature Range (°C)

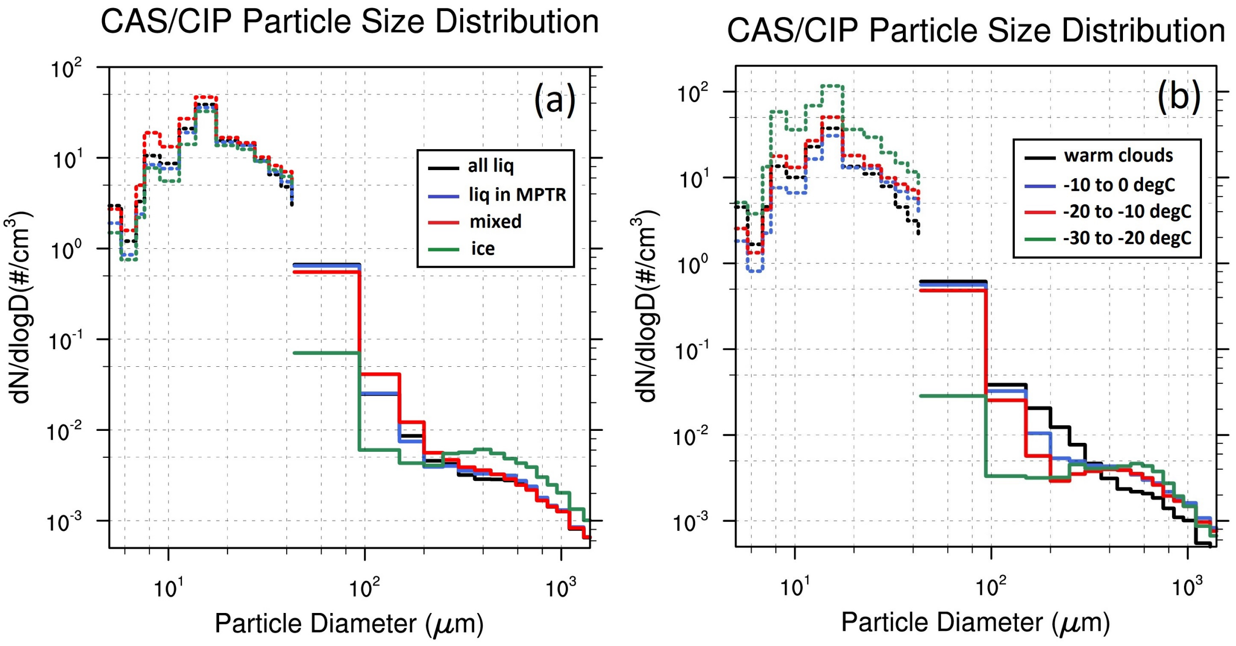
CAS/CIP Particle Size Distribution
(a)
all liq
liq in MPTR
mixed
ice
dN/dlogD(#/cm^3)
10^2
10^1
10^0
10^{-1}
10^{-2}
10^{-3}
10^1
10^2
10^3
Particle Diameter (μm)
CAS/CIP Particle Size Distribution
(b)
warm clouds
-10 to 0 degC
-20 to -10 degC
-30 to -20 degC
dN/dlogD(#/cm^3)
10^2
10^1
10^0
10^{-1}
10^{-2}
10^{-3}
10^1
10^2
10^3
Particle Diameter (μm)

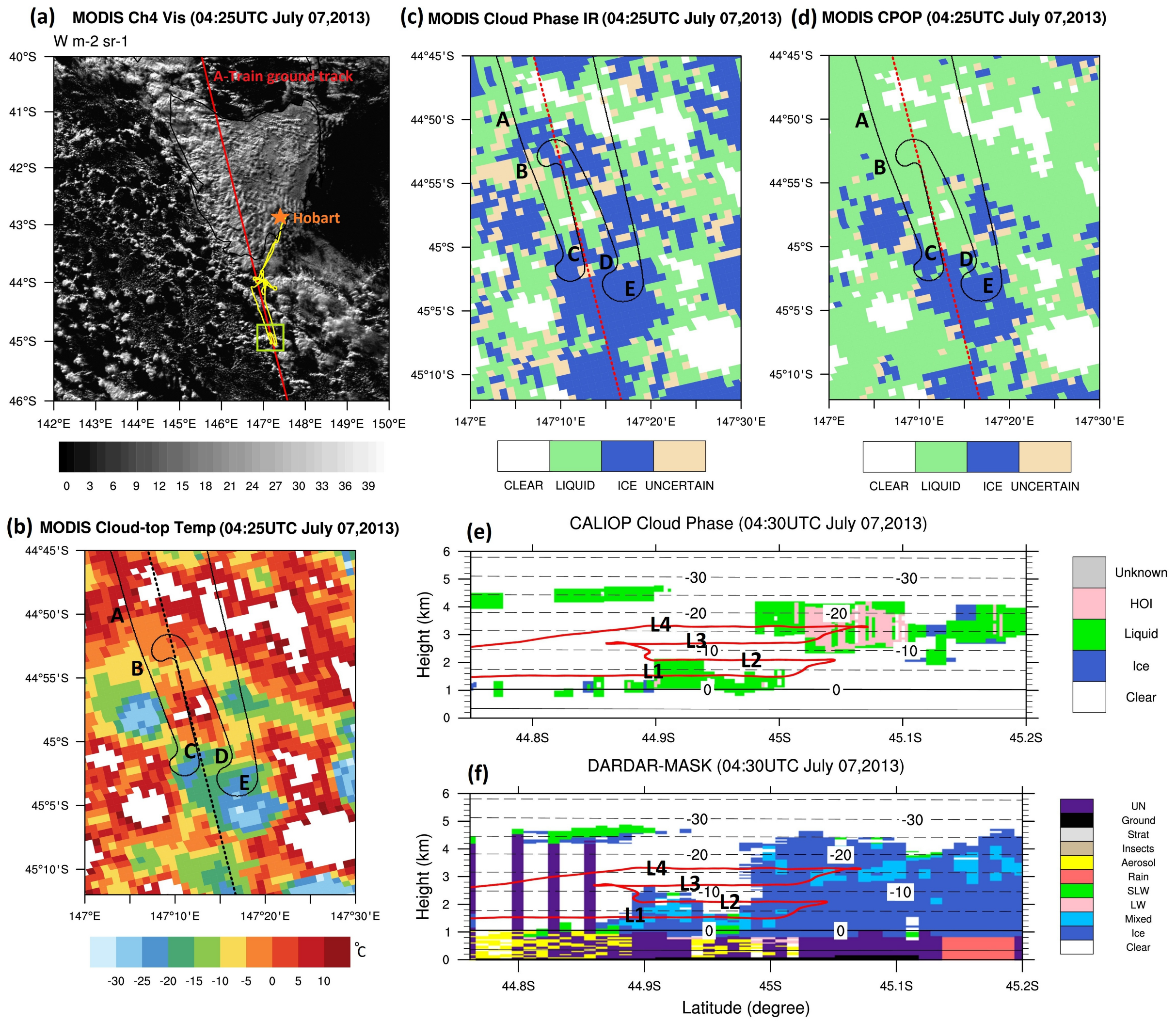
(a) MODIS Ch4 Vis (04:25UTC July 07,2013)
W m-2 sr-1
A-Train ground track
Hobart
40°S
41°S
42°S
43°S
44°S
45°S
46°S
142°E
143°E
144°E
145°E
146°E
147°E
148°E
149°E
150°E
0 3 6 9 12 15 18 21 24 27 30 33 36 39
(c) MODIS Cloud Phase IR (04:25UTC July 07,2013)
(d) MODIS CPOP (04:25UTC July 07,2013)
A
B
C
D
E
44°45'S
44°50'S
44°55'S
45°S
45°5'S
45°10'S
147°E
147°10'E
147°20'E
147°30'E
CLEAR
LIQUID
ICE
UNCERTAIN
(b) MODIS Cloud-top Temp (04:25UTC July 07,2013)
-30 -25 -20 -15 -10 -5 0 5 10
℃
(e) CALIOP Cloud Phase (04:30UTC July 07,2013)
Height (km)
-30
-20
-10
0
L1
L2
L3
L4
44.8S
44.9S
45S
45.1S
45.2S
Unknown
HOI
Liquid
Ice
Clear
(f) DARDAR-MASK (04:30UTC July 07,2013)
Latitude (degree)
UN
Ground
Strat
Insects
Aerosol
Rain
SLW
LW
Mixed
Ice
Clear

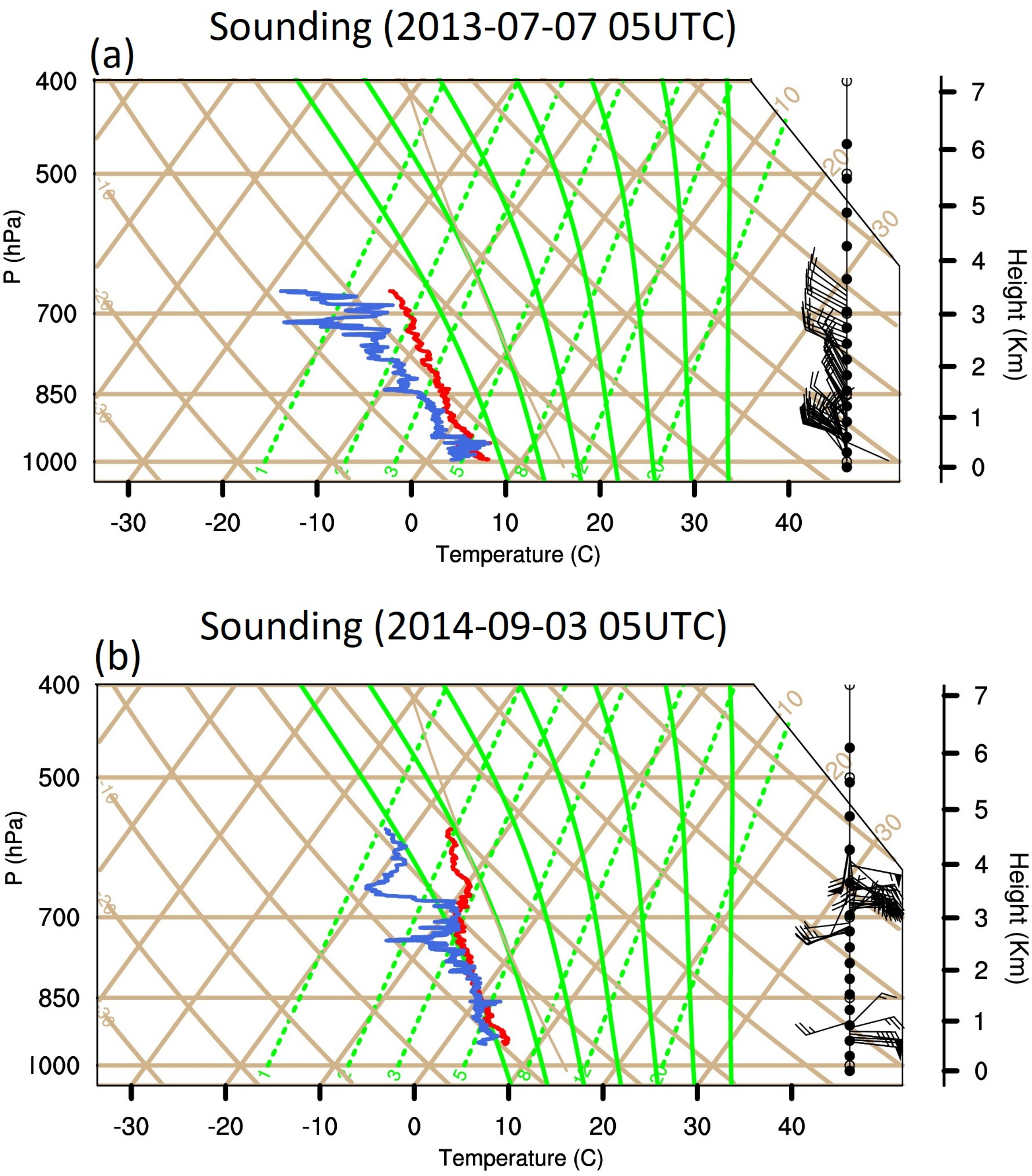

Sounding (2013-07-07 05UTC)

Sounding (2014-09-03 05UTC)

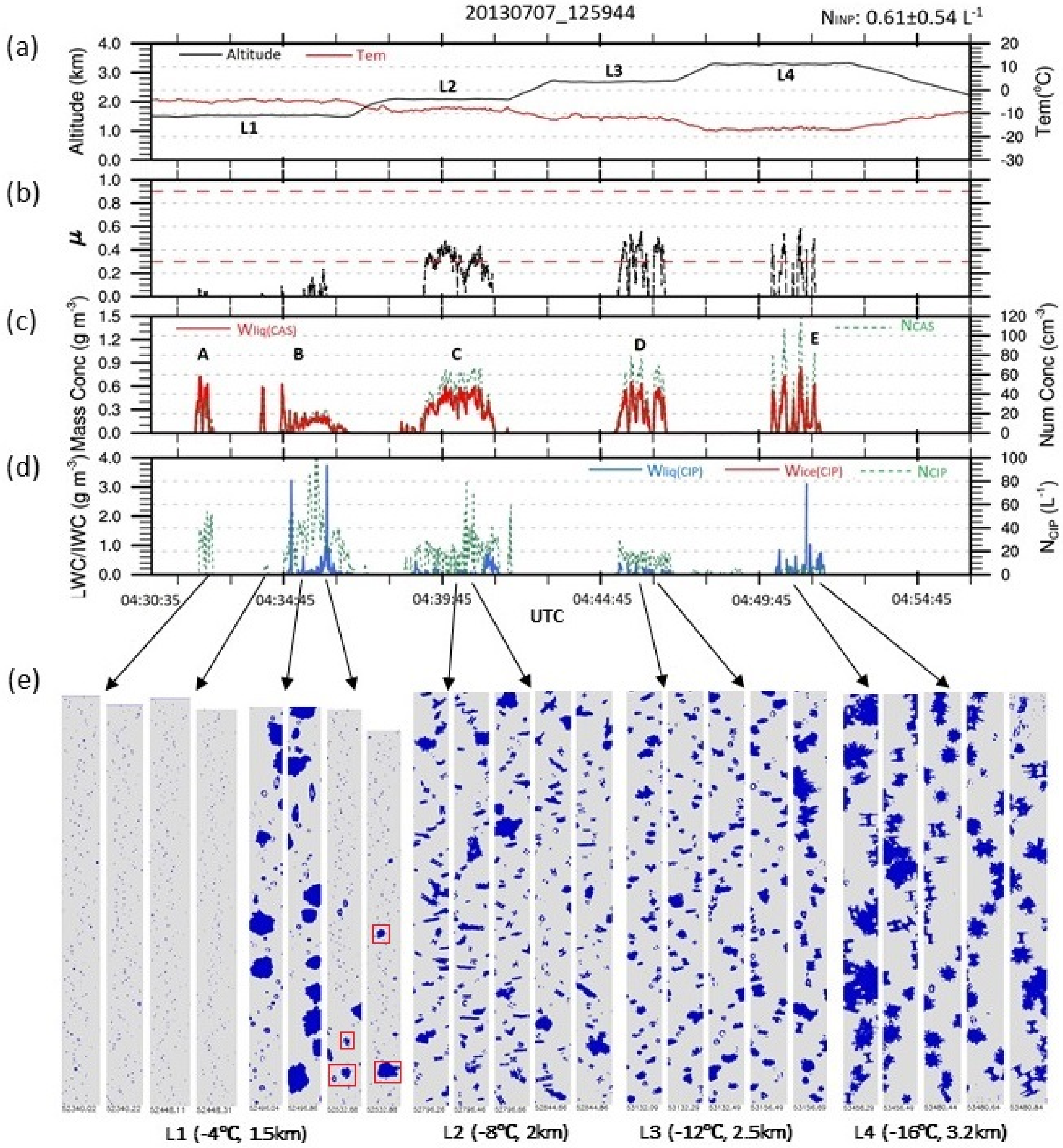
20130707_125944
NINP: 0.61±0.54 L-1
(a)
Altitude
Tem
Altitude (km)
Tem(°C)
L1
L2
L3
L4
(b)
μ
(c)
Wliq(CAS)
NCAS
A
B
C
D
E
Mass Conc (g m-3)
Num Conc (cm-3)
(d)
Wliq(CIP)
Wice(CIP)
NCIP
LWC/IWC (g m-3)
NCIP (L-1)
04:30:35
04:34:45
04:39:45
04:44:45
04:49:45
04:54:45
UTC
(e)
L1 (-4°C, 1.5km)
L2 (-8°C, 2km)
L3 (-12°C, 2.5km)
L4 (-16°C, 3.2km)

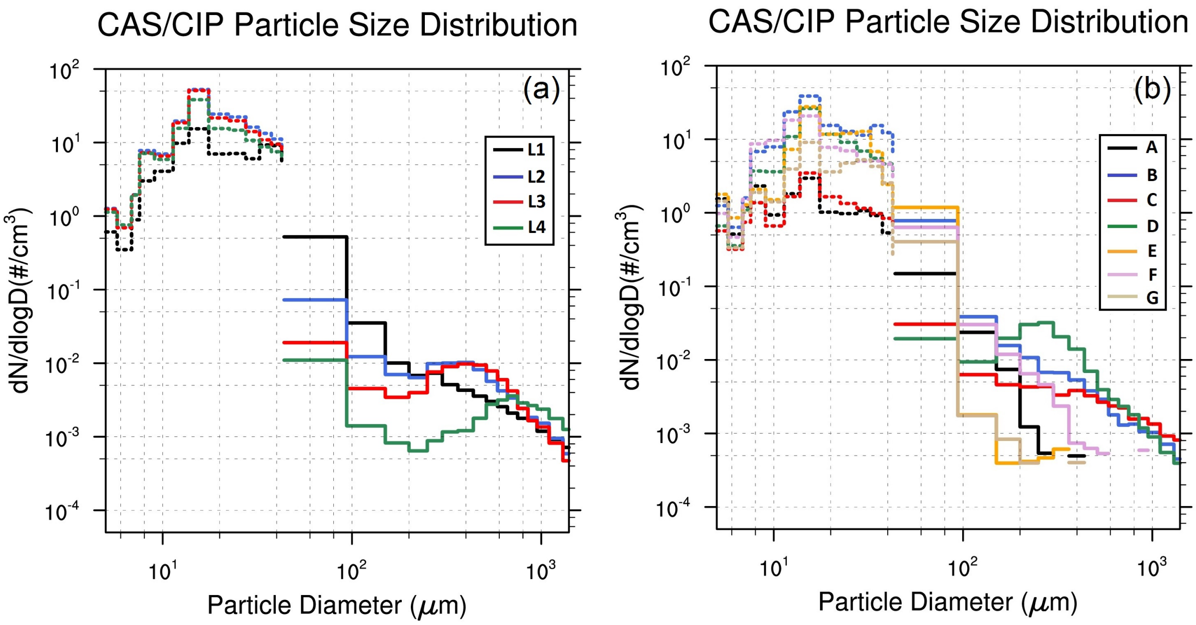
CAS/CIP Particle Size Distribution
(a)
L1
L2
L3
L4
dN/dlogD(#/cm^3)
10^2
10^1
10^0
10^{-1}
10^{-2}
10^{-3}
10^{-4}
10^1
10^2
10^3
Particle Diameter (μm)
CAS/CIP Particle Size Distribution
(b)
A
B
C
D
E
F
G
dN/dlogD(#/cm^3)
10^2
10^1
10^0
10^{-1}
10^{-2}
10^{-3}
10^{-4}
10^1
10^2
10^3
Particle Diameter (μm)

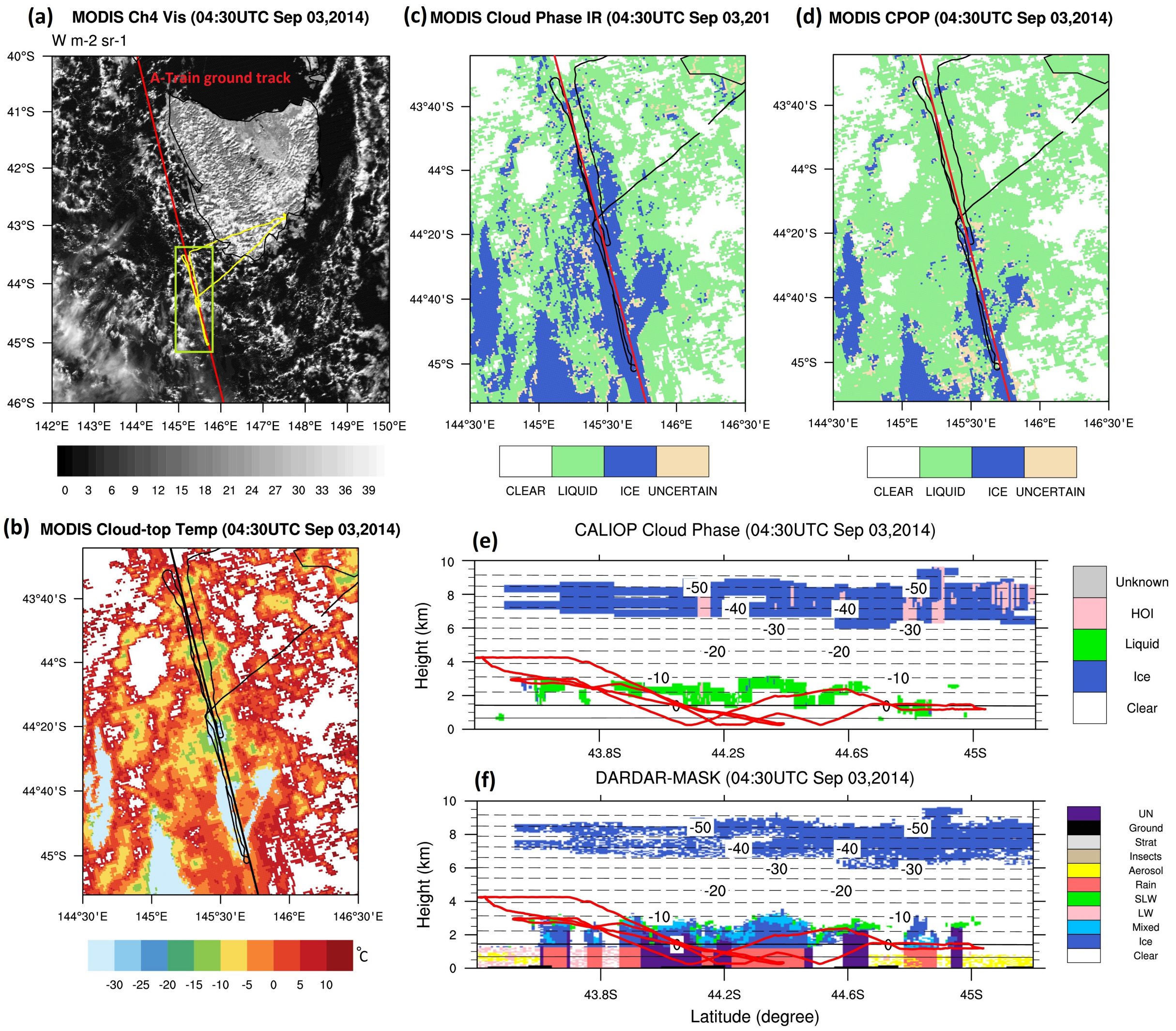
(a) MODIS Ch4 Vis (04:30UTC Sep 03,2014)
W m-2 sr-1
A-Train ground track
40°S
41°S
42°S
43°S
44°S
45°S
46°S
142°E 143°E 144°E 145°E 146°E 147°E 148°E 149°E 150°E
0 3 6 9 12 15 18 21 24 27 30 33 36 39
(c) MODIS Cloud Phase IR (04:30UTC Sep 03,201
43°40'S
44°S
44°20'S
44°40'S
45°S
144°30'E 145°E 145°30'E 146°E 146°30'E
CLEAR LIQUID ICE UNCERTAIN
(d) MODIS CPOP (04:30UTC Sep 03,2014)
43°40'S
44°S
44°20'S
44°40'S
45°S
144°30'E 145°E 145°30'E 146°E 146°30'E
CLEAR LIQUID ICE UNCERTAIN
(b) MODIS Cloud-top Temp (04:30UTC Sep 03,2014)
43°40'S
44°S
44°20'S
44°40'S
45°S
144°30'E 145°E 145°30'E 146°E 146°30'E
-30 -25 -20 -15 -10 -5 0 5 10
°C
(e) CALIOP Cloud Phase (04:30UTC Sep 03,2014)
Height (km)
10 8 6 4 2 0
-50 -40 -30 -20 -10 0
43.8S 44.2S 44.6S 45S
Unknown
HOI
Liquid
Ice
Clear
(f) DARDAR-MASK (04:30UTC Sep 03,2014)
Height (km)
10 8 6 4 2 0
-50 -40 -30 -20 -10 0
43.8S 44.2S 44.6S 45S
Latitude (degree)
UN
Ground
Strat
Insects
Aerosol
Rain
SLW
LW
Mixed
Ice
Clear

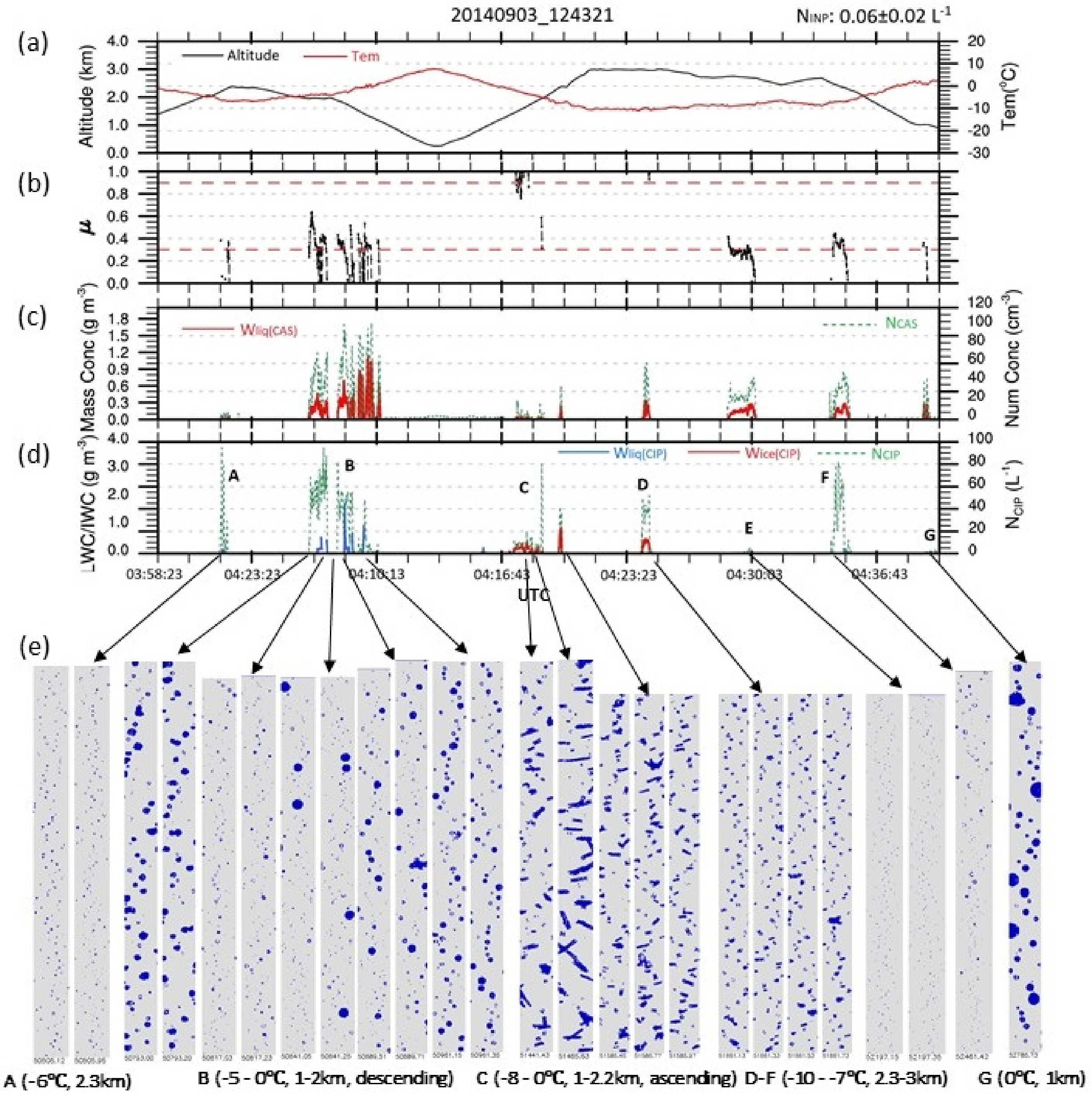
20140903_124321
N_INP: 0.06±0.02 L^-1
(a)
Altitude
Tem
Altitude (km)
Tem(°C)
(b)
μ
(c)
W_liq(CAS)
N_CAS
Mass Conc (g m^-3)
Num Conc (cm^-3)
(d)
W_liq(CIP)
W_ice(CIP)
N_CIP
LWC/IWC (g m^-3)
N_CIP (L^-1)
A
B
C
D
E
F
G
03:58:23
04:23:23
04:10:13
04:16:43
04:23:23
04:30:03
04:36:43
UTC
(e)
A (-6°C, 2.3km)
B (-5 - 0°C, 1-2km, descending)
C (-8 - 0°C, 1-2.2km, ascending)
D-F (-10 - -7°C, 2.3-3km)
G (0°C, 1km)